Geochemistry, Geophysics, Geosystems

Supporting Information for

Clumped-isotope geothermometry and carbonate U–Pb geochronology of the Alta stock metamorphic aureole, Utah, USA: Insights on the kinetics of metamorphism in carbonates

Dana C. Brenner[1], Benjamin H. Passey[2], Robert M. Holder[1,2], Daniel R. Viete[1]

[1] *Department of Earth and Planetary Sciences, Johns Hopkins University, 3400 N Charles Street, Baltimore, MD 21218, USA,* [2] *Department of Earth and Environmental Sciences, University of Michigan, Ann Arbor, MI 48109, USA*

Contents of this file

Introduction

This supporting information includes text detailing the specifics of thermal and clumped-isotope reordering models. Figures include a comparison of clumped-isotope data collected in different laboratories, field photos of outcrops within the forsterite zone, electron dispersive X-ray images and spectra for dated samples, and additional plots of clumped-isotope re-equilibration modeling, including replication of Figure 6 from main text for calcite, burial and exhumation kinetic modeling in the absence of contact metamorphism, results for the "disordered" model of Hemingway and Henkes (2020), and Monte Carlo simulations of dolomite clumped-isotope reordering kinetic parameters. Tables provide complete analytical data for clumped-isotope measurements, thermal model input parameters, and inter-laboratory comparison clumped-isotope data. The data set provides data for U–Pb analysis, available from https://archive.data.jhu.edu (also contains a high-resolution version of this document).

Text S1. Two-dimensional thermal modeling including fluid advection

Two-dimensional thermal modeling was used to explore possible thermal scenarios for the Alta stock metamorphic aureole, employing both the calcite–dolomite (Cc–Do) geothermometry results of Cook and Bowman (1994) and the carbonate clumped isotope geothermometry results of this study to constrain heating processes. The Alta stock contact metamorphic aureole experienced significant amounts of fluid infiltration (Section 1.1); previous thermal modeling studies were unable to explain Cc-Do Mg-solvus geothermometry results or oxygen isotopic data by thermal conduction alone (Cook & Bowman, 1994; Cook et al., 1997). The conduction with heat advection by fluid flow model of Cook et al. (1997), which best fit both datasets, included sub-horizontal, down-temperature fluid flow, away from the intrusion, confined by low permeability zones along the Alta–Grizzly fault, the top of the Cambrian and Mississippian carbonate unit, and the Ophir shale cap to the Tintic quartzite unit. However, this previous model did not account for the temperature dependence of thermal diffusivity and heat capacity or the latent heat of crystallization, all of which can influence the heat budget and thermal modeling results (Whittington et al., 2009; Nabelek et al., 2012). Therefore, we include these terms in our heat transport model.

We acknowledge that the thermal history of the Alta stock is more complicated than a single emplacement event and subsequent, passive cooling; instead possibly involving incremental magma emplacement, multiple thermal pulses, and/or post-emplacement hydrothermal activity (Stearns et al., 2020). However, precise constraints on timing and duration of any heating 'episodes' are not presently available, and we therefore proceed assuming the simplest (single-emplacement) scenario. Furthermore, modeling all of the complexities of advection throughout the country rock and the intrusion is beyond the scope of this study, and thus we use a model focused on lithological-layering-parallel advection within the carbonate and granodiorite units.

Conductive heat transport is represented by the equation:

$$\frac{\partial T}{\partial t} = \alpha \nabla^2 T + \frac{A}{\rho C} \qquad \text{(S1)}$$

where T is temperature in kelvins, A is an internal heating or cooling rate related to internal heat sources or sinks, t is time, ρ is density, C is specific heat capacity, and α is thermal diffusivity, expressed as:

$$\alpha = \frac{\lambda}{\rho C} \qquad \text{(S2)}$$

where λ is thermal conductivity. We modified the heat equation to include advection through the entire carbonate unit and the granodiorite intrusion, according to the heat transport equation:

$$\left[\phi\rho_f C_f + (1-\phi)\rho_s C_s\right]\frac{\partial T}{\partial t} = \nabla\cdot\left\{\left[\phi\lambda_f + (1-\phi)\lambda_s\right]\nabla T\right\} - \phi\rho_f C_f v\nabla T + A \qquad \text{(S3)}$$

after Cui et al. (2003), where subscript *f* denotes fluid and subscript *s* denotes solid, ϕ is porosity, and v is the fluid velocity following Darcy's law, as used in previous hydrodynamic studies (Cook & Bowman, 1997; Cui et al., 2001; Cui et al., 2003; Nabelek, 2009), expressed as the equation:

$$v = -\left(\frac{k}{\phi\mu}\right)\left(\nabla P - \rho_f g\right) \qquad \text{(S4)}$$

where k is intrinsic permeability, μ is the fluid dynamic viscosity, P is pressure, and g is gravity.

The heat equation is solved numerically, using an explicit finite-difference discretization in two dimensions to model the thermal profile of the contact aureole as a function of time (Carslaw & Jaeger, 1959; Furlong et al., 1991). Thermal model simulations used the geometry, grid spacing, and stratigraphic unit separations of Cook and Bowman (1994) for the same intrusion: the model was 8 km wide by 8 km deep, with grid spacing at 50 m, employing a 1.5 km half-width model of the Alta stock (Unit 5) and uniform heat flux through the boundaries. Stratigraphic units at the time of emplacement

included Cenozoic volcanics (Unit 1), minor late Paleozoic and dominant Mesozoic and Cenozoic clastic sediments (Unit 2), Paleozoic carbonates, primarily siliceous dolomite (Unit 3), and Precambrian and Cambrian quartzites (Unit 4). Table S3 shows thermal properties and depths for the stratigraphic units used in the conductive thermal model simulation.

We initialized the model with a 30 °C/km geothermal gradient, which is within the reported range of geothermal gradients (25–40 °C/km) for the Wasatch Range tectonic setting (Wilson, 1961; Kohler, 1979; Parry & Bruhn, 1986; Mayo & Loucks, 1995). The sampling transect was at 160 °C at the time of emplacement, a 5–5.5 km burial depth. We also ran a version with the sampling transect at 100 °C at the time of emplacement, following the minimum temperature scenario of Cook and Bowman (1994), which assumes either shallower burial or a lower geothermal gradient. We assumed instantaneous emplacement for the Alta stock, with a uniform temperature and pressure of 825 °C and 150 MPa, respectively. The emplacement temperature estimate was based on whole-rock zirconium geothermometry results for granodiorite magmas of Watson and Harrison (1983), which is in agreement with empirical geothermometry results of John (1991) for biotite crystallization in the Alta stock. Pressure was assumed lithostatic everywhere. Values for thermal diffusivity and heat capacity are temperature dependent (Whittington et al., 2009); therefore, we recalculated these values at each node of the model for each time step, using the equations:

$$\alpha = a \cdot \exp\left(T / b\right) + c \qquad \text{(S5)}$$

$$C = d + e \cdot T + f \cdot T^{-2} + g \cdot T^{-0.5} \qquad \text{(S6)}$$

where a, b, c, d, e, f, and g are constants determined experimentally by Nabelek et al. (2012). Thermal parameters for supercritical fluids are also highly temperature dependent. Therefore, we recalculated ρ, C, α, and μ for each time step (Lemmon et al., NIST database, *accessed November 8, 2017*). We assumed the fluid was pure H_2O and porosity was constant, using the ϕ and k values of Cook and Bowman (1994); 5% and 2.5 $\times 10^{-16}$ m^2 for carbonate and 0.5% and 0.1 $\times 10^{-16}$ m^2 for granodiorite, for porosity and

permeability, respectively. We assumed the Alta stock was impermeable prior to crystallization (<700 °C), losing heat only by conduction, and introduced fluid advection within the Alta stock only after crystallization.

The latent heat of crystallization is an important contribution to the heat budget. We therefore included, from the time of emplacement until the granodiorite of the Alta stock was assumed to have fully crystallized at 700 °C, the apparent heat capacity term recommended by Nabelek et al. (2012):

$$C_{app} = \left(\frac{T_i - T_s}{T_l - T_s}\right) C_{liq} + \left(\frac{T_i - T_s}{T_l - T_s}\right) C_{xtals} + \frac{\Delta H_f}{\left(T_l - T_s\right)} \qquad \text{(S7)}$$

where T_i is the temperature of the previous time step, T_s is the solidus temperature, T_l is the liquidus temperature, and C_{xtals} is the specific heat of the solid calculated from Eq. (6). Following Nabelek et al. (2012) and Lloyd et al. (2017), we used the thermal properties of liquid albite, for which the specific heat, C_{liq} = 1392 J/kg·K (Lange, 2003) and the latent heat of fusion, ΔH_f = 246.5 J/g (Tenner et al., 2007).

Net fluid flow is driven by the net pressure gradient, which is the sum of hydrostatic pressure gradient and the pressure gradient resulting from changing fluid densities with changing temperature. If flow is along horizontal bedding, hydrostatic pressure variation is negligible, and the net pressure gradient can be expressed as dependent primarily on temperature difference and permeability, by the equation:

$$v_z \approx \frac{k}{\phi\mu} \rho_o \alpha \Delta T g \qquad \text{(S8)}$$

where ρ_o = 1000 kg/m^3 (Norton & Cathles, 1979; Furlong et al., 1991). Highly channelized fluid flow and impermeable confining layers stratigraphically above and below (and perhaps within) the carbonate units (Woodford, 1995; Cook & Bowman, 2000) suggest that the horizontal component of fluid flow is the dominant driver of advection required to reproduce the spatial distribution of the isograds, the Cc–Do thermometry data, and oxygen isotopic data at Alta (Cook & Bowman, 1994, 2000; Cook

et al., 1997). Therefore, we ran the fluid advection model for a range of horizontal velocities in order to determine what pressure gradient best fit the Cc–Do thermometry data. We allowed the velocity to decrease, both linearly away from the Alta stock for 2 km and with time over the first 100 ky, and found an initial horizontal fluid velocity of 1×10^{-7} m/s at the contact produced the best fit. Figure 3 shows peak temperatures obtained along the sampling transect for the fluid advection model results.

We recognize that our simplified fluid advection model does not fully capture the complexities of the dynamic thermal regime at the Alta stock and surrounding area, and that numerical simulations can be sensitive to changes in thermal properties. Nevertheless, a spatial decrease in fluid flow away from the Alta stock is supported by the time-integrated fluid flux calculations, based on decarbonation reactions, of Cook and Bowman (2000). The temporal variation in fluid flow might be significantly more complex, especially considering the potential for localized hydrothermal activity during emplacement of the Little Cottonwood stock (Stearns et al., 2020), but a full investigation of the complex hydrothermal regime is beyond the scope of this study.

Text S2. Solid-state clumped isotope re-equilibration modeling

S2.1. Model structure

Here we model changes in Δ_{47} values during metamorphism and subsequent cooling, to explore whether the kinetics of clumped isotope reordering can reproduce the abrupt change in dolomite Δ_{47} values observed at the talc isograd, ~1.5 km from the Alta stock. We apply the temperature history from the 2-D fluid advective thermal model along the sampling transect (as described in Section S1). We then apply the two-stage tilting and exhumation model for the Wasatch region of Armstrong et al. (2003) to model additional changes in Δ_{47} values occurring during uplift. We recognize the thermal history of the region is potentially far more complicated than the simple emplacement, cooling, and exhumation model used here (*c.f.*, Stearns et al., 2020); however, detailed thermal reconstructions of the Alta stock contact metamorphic aureole are beyond the scope of this study.

Last, we model changes in Δ_{47} values using three kinetic models: the pseudo-first-order model of Passey and Henkes (2012), the transient-defect/equilibrium-defect model

of Henkes et al. (2014), and the exchange–diffusion model of Stolper and Eiler (2015). We also ran the disordered model of Hemingway and Henkes (2020, in review but available as a preprint from ESSOAR). Detailed description of the differences between these models is found in Stolper and Eiler (2015; see p.385–388) and recently available Hemingway and Henkes (2020). In brief, the kinetic models differ in physical interpretation of an initial period of rapid, non-first-order isotopic exchange that is observed at the onset of heating (*e.g.*, <240 minutes of heating calcite at 425 °C) in experimental studies (Passey & Henkes, 2012; Henkes et al., 2014; Stolper & Eiler, 2015; Brenner et al., 2018; Lloyd et al., 2018). The kinetic models of Passey and Henkes (2012) and Henkes et al. (2014) posit that crystallographic defects, some of which are annealable, contribute to the initial non-first-order phase of isotopic mobility. The exchange–diffusion kinetic model of Stolper and Eiler (2015) incorporates two mechanisms—an isotopic exchange with neighboring carbonate ions, resulting in the direct formation or separation of clumped isotopes, and a diffusion component, accounting for mobility of C and O at length scales greater than neighboring carbonate ion exchange. Furthermore, the exchange–diffusion model introduces the concept of a temperature-dependent preference for an overabundance of neighboring singly-isotopically-substituted carbonate ions, or pairs, whose formation and destruction could represent an integral part of clumped isotope reordering kinetics. The disordered model of Hemingway and Henkes (2020) states that all previous models are unique examples of disordered kinetics, moving from clumped isotopes to pairs, and hypothesizes that reordering kinetics can be expressed as a series of parallel first-order reactions with discrete rate constants. The authors demonstrate that all experimental data fit a lognormal distribution of rate constants for disordered reactions. The model differences are most apparent for temperature–time combinations where clumped isotope reordering conditions are only partially achieved. This range of incomplete reordering is predicted to be narrower within the framework of the kinetic models of Passey and Henkes (2012), Henkes et al. (2014), and Hemingway and Henkes (2020), but broader for the exchange–diffusion model of Stolper and Eiler (2015); (*e.g.*, Brenner et al., 2018; Fig. 6).

Models were run using both the kinetic parameters of calcite under the wet, high-pressure conditions of Brenner et al. (2018) and the kinetic parameters of dolomite from

Lloyd et al. (2018) using both an original MATLAB program and the ClumpyCool python program of Lloyd (2020). The disordered model was run using the 'isotopolog' python package (Hemingway, 2020) with rate constants of Hemingway and Henkes (2020). In order to eliminate potential error associated with temperature calibration, we used the universal carbonate calibration of Bonifacie et al. (2017) for both calcite and dolomite. Figure 6a–c,g–i shows modeled Δ_{47} values with distance from the Alta stock, after various cooling times between 5,000 yr and 500,000 yr, for each of the pseudo-first-order, transient-defect/equilibrium-defect, and paired reaction–diffusion models. Profiles for actual temperature are shown in Fig. S17 and dolomite results for the disordered model of Hemingway and Henkes (2020) are shown in Fig. S18. Modeling results using calcite kinetics are shown in Fig. S19–S20. For both the calcite and dolomite kinetic parameters used, the stepped profile of modeled clumped isotope values is sharpest for the shortest cooling time, and flattens with increasing duration of cooling. Model runs based on calcite kinetics predict extensive modification of Δ_{47} values well beyond the talc isograd, and produce a relatively gentle Δ_{47} value gradient after 500,000 yr. The flattened profiles of all models using calcite kinetics fail to maintain the stepped profile observed in the dolomite Δ_{47} values surrounding the Alta stock (Fig. S19–S20). All kinetic models fall within the range of $T(\Delta_{47})$ values observed in calcite, but underestimate $T(\Delta_{47})$ of calcite at the contact (Table 1, Fig. S19–S20).

S2.2. Modeling results using kinetic parameters from experimental studies

All kinetic models capture the distinct step feature observed in dolomite Δ_{47} values to some extent (Fig. 6, S18–S20). However, the precise location of the stepped-feature is dependent on the model used; all predicted the break beyond the talc isograd, outside the metamorphic aureole. This suggests that, for the cooling scenario at the Alta stock contact metamorphic aureole, clumped isotope re-equilibration was extremely temperature sensitive, and that, although different kinetic models predict different blocking temperatures, for temperatures beyond the blocking value, atomic mobility was efficient. The steep slope reproduced in the dolomite-modeled Δ_{47} values stabilizes after 200,000 yr at distances of ~2.3 km and ~2.5 km from the Alta stock, for the pairs exchange-diffusion and pseudo-first-order models, respectively. This feature in

dolomite-modeled Δ_{47} values persists (maintaining the sharp break) with continued passive cooling from 200,000 yr to 500,000 yr and throughout the exhumation history. Dolomite-modeled Δ_{47} values for all samples bifurcate: carbonates within the thermal aureole, from the contact with the Alta stock to the observed break in dolomite Δ_{47} values, converge on a similar cooling-rate-dependent Δ_{47} value during exhumation, regardless of distance from the contact; carbonates beyond the abrupt jump in dolomite Δ_{47} values similarly converge on a lower cooling-rate-dependent Δ_{47} value than samples within the thermal aureole. Figure 6d–f,j–l shows Δ_{47} values with time after emplacement of the Alta stock (including subsequent tilting and exhumation) and $T(\Delta_{47})$ profiles for distances 0.05–6.5 km away from the Alta stock, based on dolomite kinetics.

Final dolomite-modeled Δ_{47} values fail to capture the observed dolomite $T(\Delta_{47})$ values in the thermal aureole. Model results for the pairs exchange-diffusion and pseudo-first-order each predict the break in dolomite Δ_{47} values ~1 km farther down temperature than was observed. In order to achieve $T(\Delta_{47})$ >350 °C within the thermal aureole and at the talc isograd using the dolomite kinetic parameters of Lloyd et al. (2018), cooling rates of ~10^7–10^8 °C/My are required. These cooling rates are geologically implausible.

S2.3. Constraints from the Alta stock on dolomite clumped isotope kinetic parameters

There are three main explanations for the misfit of clumped isotope modeling results to observed dolomite Δ_{47} values; the thermal history at the Alta stock is significantly different than captured by the thermal model of this study; current clumped-isotope re-equilibration models and existing kinetic parameters do not adequately capture C and O mobility, and thus clumped isotope reordering, at the Alta stock; or some other processes (e.g., diagenesis) have influenced the clumped isotope abundances of dolomite samples surrounding the Alta stock.

It seems unlikely that, with the absence of obvious structural changes or changes in porosity and/or texture, additional processes such as diagenesis, subsequent recrystallization, or dolomitization should preferentially affect dolomite within the thermal aureole. The possibility of recrystallization is discussed in Section 4.1.2 and does not appear to be a viable explanation for the observed step in dolomite clumped

isotope abundances. Effects from prior solid-state alteration of clumped-isotope abundances, for example an earlier thermal perturbation, may have influenced the re-equilibration of clumped isotopes in dolomite during a subsequent thermal event. For example, at the Ballachulish aureole in Scotland, Beyssac et al. (2019) observed that pretransformation of carbonaceous material during regional metamorphism c. 45 Ma prior to intrusion yielded more sluggish subsequent ordering of graphitic carbon during contact metamorphism associated with emplacement. However, there is no documentation or indication that mobilization of C and O isotopes in carbonates should behave in a similar manner; although, further investigation of this possibility is warranted. Nevertheless, we assume that this would have a dampening effect, or attenuate the change in dolomite clumped isotope abundances, rather than maintain the sharp change in dolomite Δ_{47} values observed at the Alta stock.

The thermal history of the Alta stock contact metamorphic aureole is unquestionably more complex than the simple, single magma emplacement episode (with fluid advection) and subsequent cooling and exhumation model presented in this study. For example, Stearns et al. (2020) hypothesized the existence of a persistent plumbing system throughout Alta during the emplacement history of the Little Cottonwood stock that channelized hydrothermal fluids from newly emplacement intrusions toward older intrusions, allowing prolonged durations of heating. Nevertheless, multiple thermal pulses still require unrealistically quick cooling rates of ~10^7–10^8 °C/My, using the kinetic parameters of Lloyd et al. (2018), to retain the observed dolomite Δ_{47} values. This agrees with the range of range of $T(\Delta_{47})$ for various cooling rates of Hemingway and Henkes (2020; see Fig.5). Furthermore, if the thermal model parameters are adjusted to the extent that the kinetic model and parameters of Lloyd et al. (2018) reproduce the observed step in dolomite Δ_{47} values, the resulting thermal history predicts peak temperature at the talc isograd <300 °C, which is not reasonable for talc formation. This adjusted thermal model also yields unrealistically low temperatures for the periclase, forsterite, and tremolite isograds. We therefore assume that the 2-D thermal model of this study adequately captures the major thermal events influencing carbonate clumped isotope reordering.

Different clumped-isotope kinetic models, based on different rate equations, capture, to some extent, the observed step behavior of the dolomite Δ_{47} values, but the stepped profile of modeled results does not spatially align with observations. We therefore assume that the kinetic models are capturing the observed behavior and consider the possibility that the kinetic parameters might not be appropriate for the Alta stock thermal regime. We proceed to investigate possible kinetic parameters that can reproduce the profile observed in dolomite Δ_{47} values at the Alta stock contact metamorphic aureole, with the assumption that the thermal model, the thermal parameters, and the kinetic models used in this study are all adequately reflecting the thermal regime along the sampling transect. In heating regimes where the blocking temperature is far exceeded (*i.e.*, the abundance of clumped isotopes approaches stochastic distribution) and cooling rates are sufficiently high (on the order of $\sim 10^4$ °C/My), such as for the Alta stock and other rapidly cooling contact metamorphic environments, the cooling process should have greater influence on the final Δ_{47} value. In these scenarios, the abundance of clumped isotopes transitions from a disordered, high-temperature (>>blocking temperature) arrangement — a stochastic distribution of clumped isotopes—to a more ordered, lower-temperature abundance of clumped isotopes. This distinction is important because, to date, the dominant application of carbonate clumped isotope geothermometry has been to thermal regimes significantly below the blocking temperature. In the Alta stock contact metamorphic aureole, and in similar cooling-dominated thermal regimes occurring over geologic timescales, subtle differences observed in experimental heating studies (*e.g.*, initial rapid reordering phases) should not exert significant influence on prolonged solid-state isotopic mobility. Instead, in these rapidly cooling scenarios, slow solid-state diffusion *via* first-order kinetic behavior, which has been observed in all re-equilibration experimental studies, will control final dolomite Δ_{47} values.

With this assumption, we proceed by modeling changes in dolomite Δ_{47} values using a simplified pseudo-first-order kinetic model and evaluate a range of potential kinetic parameters for dolomite that could reproduce the break in dolomite Δ_{47} values observed in the contact metamorphic aureole at Alta. We ran 10,000 Monte Carlo simulations of the pseudo-first-order kinetic model, randomly varying activation energies

E_a and pre-exponential factors k; guidance for potential dolomite re-equilibration kinetic parameters was taken from Lloyd et al. (2018), using activation energy E_a = 50–300 kJ and pre-exponential factor $k = 1\times10^4 - 1\times10^{13}$ s^{-1}. We then defined a fit to observed dolomite Δ_{47} values as satisfying both Δ_{47} value <0.260 and Δ_{47} value >0.340 at distances of 1.4 km and 1.9 km from the contact, respectively. We evaluated the fit of each paired E_a and k combination to dolomite Δ_{47} values observed at the Alta stock, and used the combination of E_a and k values that best produced the mean sigmoidal profile (E_a = 300 kJ and $k = 1.0102\times10^{12}$ s^{-1}). Modeled Δ_{47} values using these E_a and k combinations are shown in the Fig. S21.

Figure S22 shows modeled dolomite Δ_{47} values using the pseudo-first-order kinetic model and the optimal dolomite kinetic parameter pair from Monte Carlo simulations (E_a = 300 kJ and $k = 1.0102\times10^{12}$ s^{-1}). Modeled dolomite Δ_{47} values ≤1 km from the contact converge on a similar cooling-rate-dependent Δ_{47} value. At distances >2 km from the contact there is no equivalent observable change in Δ_{47} values; presumably because temperatures never exceeded the blocking temperature for dolomite for the cooling rates experienced. At the talc isograd, 1.5 km away from the Alta stock, modeled Δ_{47} values stabilize at a higher Δ_{47} value than modeled Δ_{47} values at distances closer to the contact (0.269‰ CDES90 and 0.222‰ CDES90, respectively). This suggests the peak temperature reached at the talc isograd is near the blocking temperature of dolomite for the cooling rate experienced.

Our model does not explain the variability in Δ_{47} values for calcite and dolomite close to the Alta stock (≤0.5 km). One possible explanation is that samples within 0.5 km of the Alta stock experienced secondary alteration, after initial emplacement and cooling of the Alta stock. If late hydrothermal activity at the Alta stock was coeval with Little Cottonwood Stock emplacement (Stearns et al., 2020), the dolomite samples <0.5 km from the Alta stock could have been thermally reset to higher Δ_{47} values, corresponding to lower apparent equilibrium temperatures. A larger issue is that these kinetic parameters are significantly outside those determined from controlled heating experiments and highlights an aspect of reordering models that warrants further investigation. Additional high temperature data and dolomite specific heating experiments as well as optimization

for both experimental observations and constraints from regional and contact metamorphism will improve utility of current reordering models.

Figure S23 shows dolomite kinetic modeling results for a theoretical simple burial and exhumation history in the absence of contact metamorphism. Burial history assumes a maximum burial temperature of 160 °C, and the exhumation history is after Armstrong et al. (2003), the same as the other kinetic modeling. The disordered model yields completed reordered dolomite with final $T(\Delta_{47})$ reflecting the maximum burial temperature of 160 °C. However, the exchange-diffusion model predicts dolomite is only partially reordered to final $T(\Delta_{47})$ ~80 °C, significantly below the $T(\Delta_{47})$ ~160 °C observed. It is possible that dolomite beyond the talc isograd was partially reordered in response to contact metamorphism, not burial alone. This agrees with the theoretical basis of the exchange–diffusion kinetic model wherein the concentration of pairs can buffer continued reordering (see Stolper & Eiler, 2015, p. 388). The talc isograd might spatially represent the thermal threshold between complete reordering and partial reordering due to pair saturation. In this scenario, there was sufficient energy for complete reordering inside the metamorphic aureole. However, outside the metamorphic aureole there was insufficient energy to separate pairs and the increasing pairs concentration prevented complete re-equilibration. Alternatively, the $T(\Delta_{47})$ ~160 °C of dolomite beyond the talc isograd might represent some post-depositonal (re)crystallization that occurred at 160 °C, prior to emplacement of the Alta stock. It is possible that a single event (*e.g.*, dolomitization) is responsible for both the consistent ~35 Ma dolomite U–Pb date and the observed $T(\Delta_{47})$ ~160 °C beyond the talc isograd.

Carbonates experiencing rapidly-cooling scenarios ($\geq 10^4$ °C/My) record significantly higher temperature alterations in both calcite and dolomite than slower-cooling scenarios ($\leq 10^3$ °C/My), which may only record thermal perturbations in dolomite, not calcite. For example, Lloyd et al. (2017) observed maximum apparent equilibrium temperatures within the Notch Peak thermal aureole of 177^{+15}_{-13} °C (1 σ) and 348^{+22}_{-20} °C (1 σ) for calcite and dolomite, respectively, for a cooling rate of ~10^3 °C/My compared with 257^{+30}_{-25} °C (95% C.I.) and 422^{+84}_{-61} °C (95% C.I.) for calcite at the contact and dolomite within the inner aureole, respectively, for the Alta stock cooling rate of

~10^4 °C/My. [Cooling rates of 5.0×10^4 °C/My and 2.3×10^4 °C/My were calculated for the Alta stock using Eq. (14) of Passey and Henkes (2012) and the kinetic parameters of calcite under wet, high pressure conditions of Brenner et al. (2018) and dolomite from Monte Carlo simulations of this study, respectively]. This suggests that the Alta stock Δ_{47} values record contact-metamorphic thermal signatures in both calcite and dolomite and implies that cooling rate is the dominant control on final clumped-isotope abundances in carbonates of similar peak metamorphic temperature.

Text S3. References

Armstrong, P. A., Ehlers, T. A., Chapman, D. S., Farley, K. A., & Kamp, P. J. J. (2003). Exhumation of the central Wasatch Mountains, Utah: 1. Patterns and timing of exhumation deduced from low-temperature thermochronology data. *Journal of Geophysical Research, 108*(B3), 2172. https://doi.org/10.1029/2001JB001708

Beyssac, O., Pattison, D. R. M., & Bourdelle, F. (2018). Contrasting degrees of recrystallization of carbonaceous material in the Nelson aureole, British Columbia and Ballachulish aureole, Scotland, with implications for thermometry bassed on Raman spectroscopy of carbonaceous material. *Journal of Metamorphic Geology, 37*, 71–95. https://doi.org/10.1111/jmg.12449

Bonifacie, M., Calmels, D. Eiler, J. M., Horita, J., Chaduteau, C., Vasconcelos, C., et al. (2017). Calibration of the dolomite clumped isotope thermometer from 25 to 350 °C, and implications for a universal calibration for all (Ca, Mg, Fe)CO_3 carbonates. *Geochimica et Cosmochimica Acta*, *200*, 255–279.

Brenner, D. C., Passey, B. H., & Stolper, D. A. (2018). Influence of water on clumped isotope bond reordering kinetics in calcite. *Geochimica et Cosmochimica Acta, 224*, 42–63. https://doi.org/10.1016/j.gca.2017.12.026

Carslaw, H. S., & Jaeger, J. C. (1959). *Conduction of heat in solids* (2nd ed.). New York, NY: Oxford University Press.

Cook, S. J., & Bowman, J. R. (1994). Contact metamorphism surrounding the Alta stock: Thermal constraints and evidence of advective heat transport from calcite + dolomite geothermometry. *American Mineralogist, 79*, 513–525.

Cook, S. J., & Bowman, J. R. (2000). Mineralogical evidence for fluid-rock interaction

accompanying prograde contact metamorphism of siliceous dolomites: Alta stock aureole, Utah, USA. *Journal of Petrology, 41*(6), 793–757. https://doi.org/10.1093/petrology/41.6.739

Cook, S. J., Bowman, J. R., & Forster, C. B. (1997). Contact metamorphism surrounding the Alta stock: Finite element model simulation of heat- and $^{18}O/^{16}O$ mass-transport during prograde metamorphism. *American Journal of Science, 297*(1), 1–55. https://doi.org/10.2475/ajs.297.1.1

Cui, X., Nabelek, P. I., & Liu, M. (2001). Heat and fluid flow in contact metamorphic aureoles with layered and transient permeability, with application to the Notch Peak aureole, Utah. *Journal of Geophysical Research, 106*(B4), 6477–6491. https://doi.org/10.1029/2000jb900418

Cui, X., Nabelek, P. I., & Liu, M. (2003). Reactive flow of mixed CO_2–H_2O fluid and progress of calc-silicate reactions in contact metamorphic aureoles: insights from two-dimensional numerical modeling. *Journal of Metamorphic Geology, 21*(7), 663–684. https://doi.org/10.1046/j.1525-1314.2003.00475.x

Furlong, K. P., Hanson, R. B., & Bowers, J. R. (1991). Modelling thermal regimes. In D. M. Kerrick (ed.), *Contact metamorphism* (Vol. 26, pp. 437–505). Washington, DC: Mineralogical Society of America.

Hasterok, D., & Webb., J. (2017). On the radiogenic heat production of igneous rocks. *Geoscience Frontiers 8*, 919–940. https://doi.org/10.1016/j.gsf.2017.03.006

Hemingway, J. D. (2020). Isotopylog: Open-source tools for clumped isotope kinetic data analysis. http://pypi.python.org/pypi/isotopylog

Hemingway, J. D. & Henkes, G. A. (2020). A distributed activation energy model for clumped isotope bond reordering in carbonates. *Earth and Space Science Open Archive.* https://doi.org/10.1002/essoar.10504096.1

Henkes, G. A., Passey, B. H., Grossman, E. L., Shenton, B. J., Pérez-Huerta, A., & Yancey, T. E. (2014). Temperature limits for preservation of primary calcite clumped isotope paleotemperatures. *Geochimica et Cosmochimica Acta, 139*, 362–382. https://doi.org/10.1016/j.gca.2014.04.040

John, D. A. (1991). Evolution of hydrothermal fluids in the Alta stock, Central Wasatch Mountains, Utah. *U. S. Geological Survey Bulletin, 1977*. https://doi.org/10.3133/b1977

Kohler, J. F. (1979). Geology, characteristics, and resource potential of the low-temperature geothermal system near Midway, Wasatch County, Utah. *All U.S. Government Documents (Utah Regional Despository)*. Paper 54.

Lange, R. A. (2003). The fusion curve of albite revisited and the compressibility of $NaAlSi_3O_8$ liquid with pressure. *American Mineralogist, 88*(1), 109–120. https://doi.org/10.2138/am-2003-0114

Lemmon, E. W., McLinden, M. O., & Friend, D. G. Thermophysical properties of fluid systems. In P. J. Linstrom & W. G. Mallard (Eds.), *NIST Chemistry WebBook, NIST Standard Reference Database Number 69* Gaithersburg, MD: National Institute of Standards and Technology. doi: 10.18434/T4D303

Lloyd, M. K. (2020). ClumpyCool. *Open Science Framework*. https://doi:10.17605/OSF.IO/JYHSW

Lloyd, M. K., Eiler, J. M., & Nabelek, P. I. (2017). Clumped isotope thermometry of calcite and dolomite in a contact metamorphic environment. *Geochimica et Cosmochimica Acta, 197*, 323–344. https://doi.org/10.1016/j.gca.2016.10.037

Lloyd, M. K., Ryb, U., & Eiler, J. M. (2018). Experimental calibration of clumped isotope reordering in dolomite. *Geochimica et Cosmochimica Acta, 242*, 1–20. https://doi.org/10.1016/j.gca.2018.08.036

Mayo, A. L., & Loucks, M. D. (1995). Solute and isotopic geochemistry and ground water flow in the central Wasatch Range, Utah. *Journal of Hydrology, 172*(1–4), 31–59. https://doi.org/10.1016/0022-1694(95)02748-e

Nabelek, P. I. (2009). Numerical simulation of kinetically-controlled calc-silicate reactions and fluid flow with transient permeability around crystallizing plutons. *American Journal of Science, 309*(7), 517–548. https://doi.org/10.2475/07.2009.01

Nabelek, P. I., Hofmeister, A. M., & Whittington, A. G. (2012). The influence of temperature-dependent thermal diffusivity on the conductive cooling rates of

plutons and temperature-time paths in contact aureoles. *Earth and Planetary Science Letters, 317–318*, 157–164. https://doi.org/10.1016/j.epsl.2011.11.009

Norton, D., & Cathles, L. M. (1979). Thermal aspects of ore deposition. In *Geochemistry of hydrothermal ore deposits* (Vol. 2, pp. 611–631). New York, NY: Wiley.

Parry, W. T., & Bruhn, R. L. (1986). Pore fluid and seismogenic characteristics of fault rock at depth on the Wasatch fault, Utah. *Journal of Geophysical Research, 91*(B1), 730–744. https://doi.org/10.1029/jb091ib01p00730

Passey, B. H., & Henkes, G. A. (2012). Carbonate clumped isotope bond reordering and geospeedometry. *Earth and Planetary Science Letters, 351–352*, 223–236. https://doi.org/10.1016/j.epsl.2012.07.021

Stearns, M. A., Bartley, J. M., Bowman, J. R., Forster, C. W., Beno, C. J., Riddle, D. D., Callis, S. J., & Udy, N. D. (2020). Simultaneous magmatic and hydrothermal regimes in Alta-Little Cottonwood Stocks, Utah, USA, recorded using multiphase U-Pb petrochronology. *Journal of Geosciences, 10*(4), 129. https://doi.org/10.3390/geosciences10040129

Stolper, D. A., & Eiler, J. M. (2015). The kinetics of solid-state isotope-exchange reactions for clumped isotopes: A study of inorganic calcites and apatites from natural and experimental samples. *American Journal of Science, 315*(5), 363–411. https://doi.org/10.2475/05.2015.01

Tenner, T. J., Lange, R. A., Downs, R. T. (2007). The albite fusion curve reexamined: new experiments and the high-pressure density and compressibility of high albite and $NaAlSi_3O_8$ liquid. *American Mineralogist, 92*, 1573–1585. https://doi.org/10.2138/am.2007.2464

Vilà, M., Fernández, M., & Jiménez-Munt, I. (2010). Radiogenic heat production variability of some common lithological groups and its significance to lithospheric thermal modeling. *Tectonophysics, 490*(3–4), 152–164. https://doi.org/10.1016/j.tecto.2010.05.003

Watson, E. B., & Harrison, T. M. (1983). Zircon saturation revisited: Temperature and composition effects in a variety of crustal magma types. *Earth and Planetary Science Letters*, *64*(2), 295–304. https://doi.org/10.1016/0012-821x(83)90211-x

Whittington, A. G., Hofmeister, A. M., & Nabelek, P. I. (2009). Temperature-dependent

thermal diffusivity of Earth's crust and implications for magmatism. *Nature, 458*(7236), 319–321. https://doi.org/10.1038/nature07818

Wilson, J. W. (1961). *Geology of the Alta stock* (Doctoral dissertation). Retrieved from Caltech THESIS. (https://resolver.caltech.edu/CaltechTHESIS:04112011-153508154). Pasedena, CA: California Institute of Technology.

Woodford, D. T. (1995). *Boron metasomatism in the Alta stock thermal aureole, Alta, Utah* (Master's thesis). Retrieved from Rice University Electronic Theses and Dissertations. (https://hdl.handle.net/1911/14009). Houston, TX: Rice University.

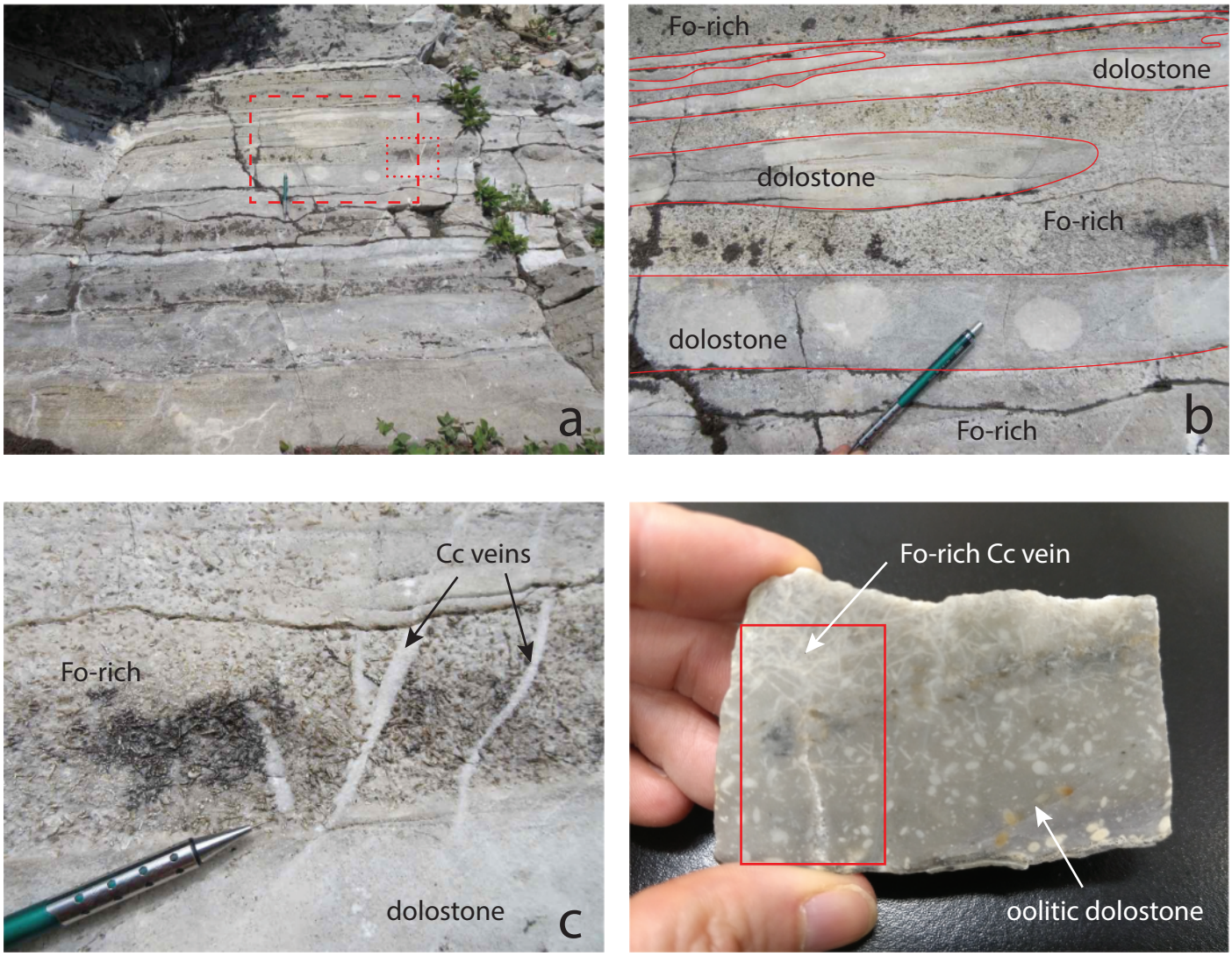

Figure S1. Photographs taken 0.5 km from the Alta stock of AS17-73 sampling location and hand specimen. a) Outcrop scale photograph illustrating prominent bedding planes alternating between dolostone with minor and prolific forsterite (Fo) occurrence. Mechanical pencil in the middle of the photograph for scale. Large red, dashed-line box is shown in (b) and small red, dotted-line box is shown in (c). b) Zoom in of large dashed-line box in (a) illustrating dolostone lenses with minor Fo and Fo-rich layers; layers outlined in red. c) Zoom in of small dotted-line box in (a) focused on contact between dolostone with minor occurrence of Fo and Fo-rich layer. Prominent calcite (Cc) veins cross-cutting the center and right side of photograph. d) Photograph of hand specimen with Fo-rich Cc vein starting at bottom left and fanning out at upper left portion of sample. Lower portion of sample is oolitic dolostone. Red, solid-line box indicates location of thin section shown in Fig. S3, S14.

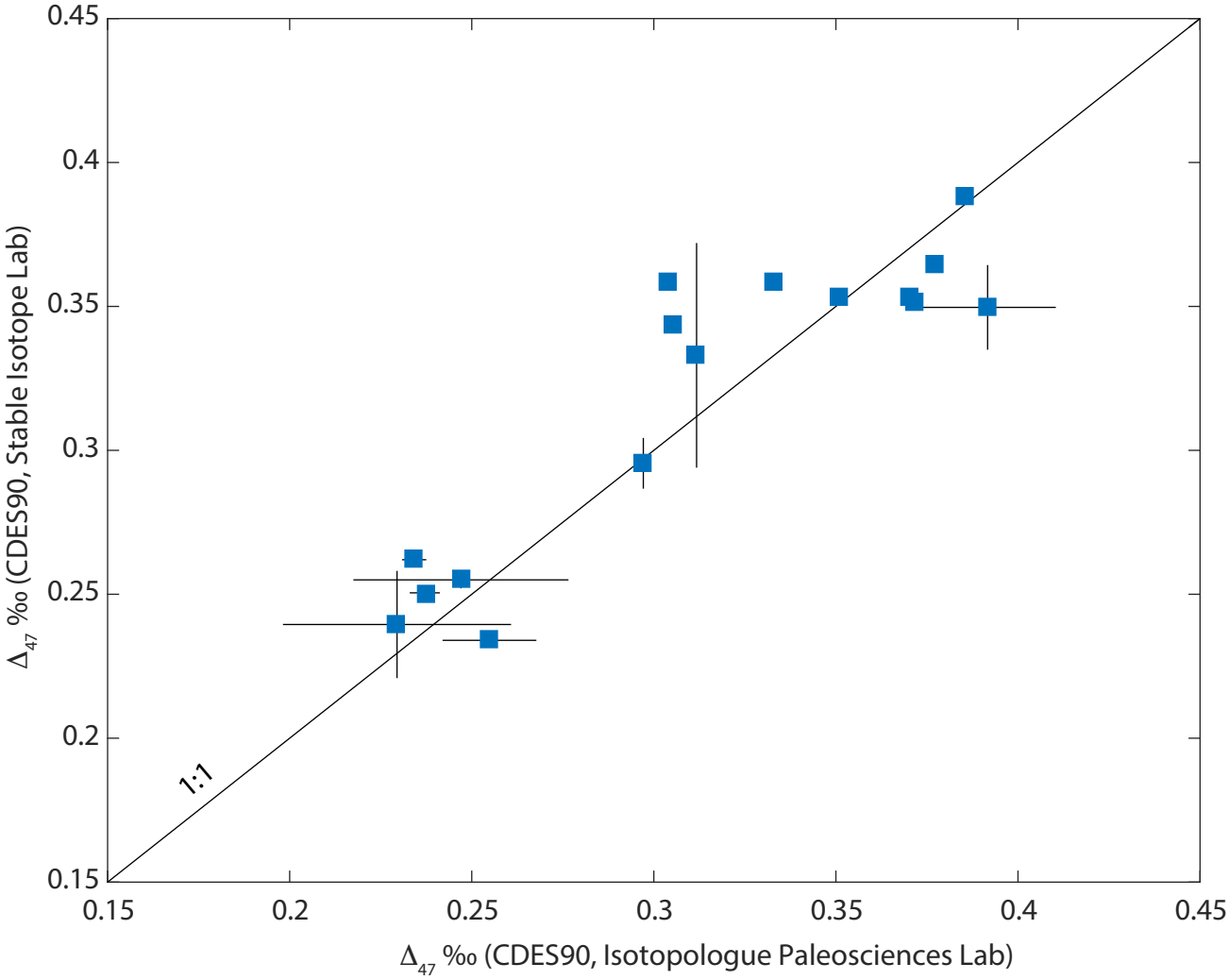

Figure S2. Plot of Δ_{47} values for samples analyzed in the Isotopologue Paleosciences Lab versus the Stable Isotope Lab. The Δ_{47} values are average values for replicates from a single lab reported in the carbon dioxide equilibrium scale (CDES) of Dennis et al. (2011) as the 90 °C (CDES90) acid digestion value recommended by Bonifacie et al. (2017) . Error bars represent the 95% C.I. for replicate analyses for a single lab. The solid line represents a one-to-one line.

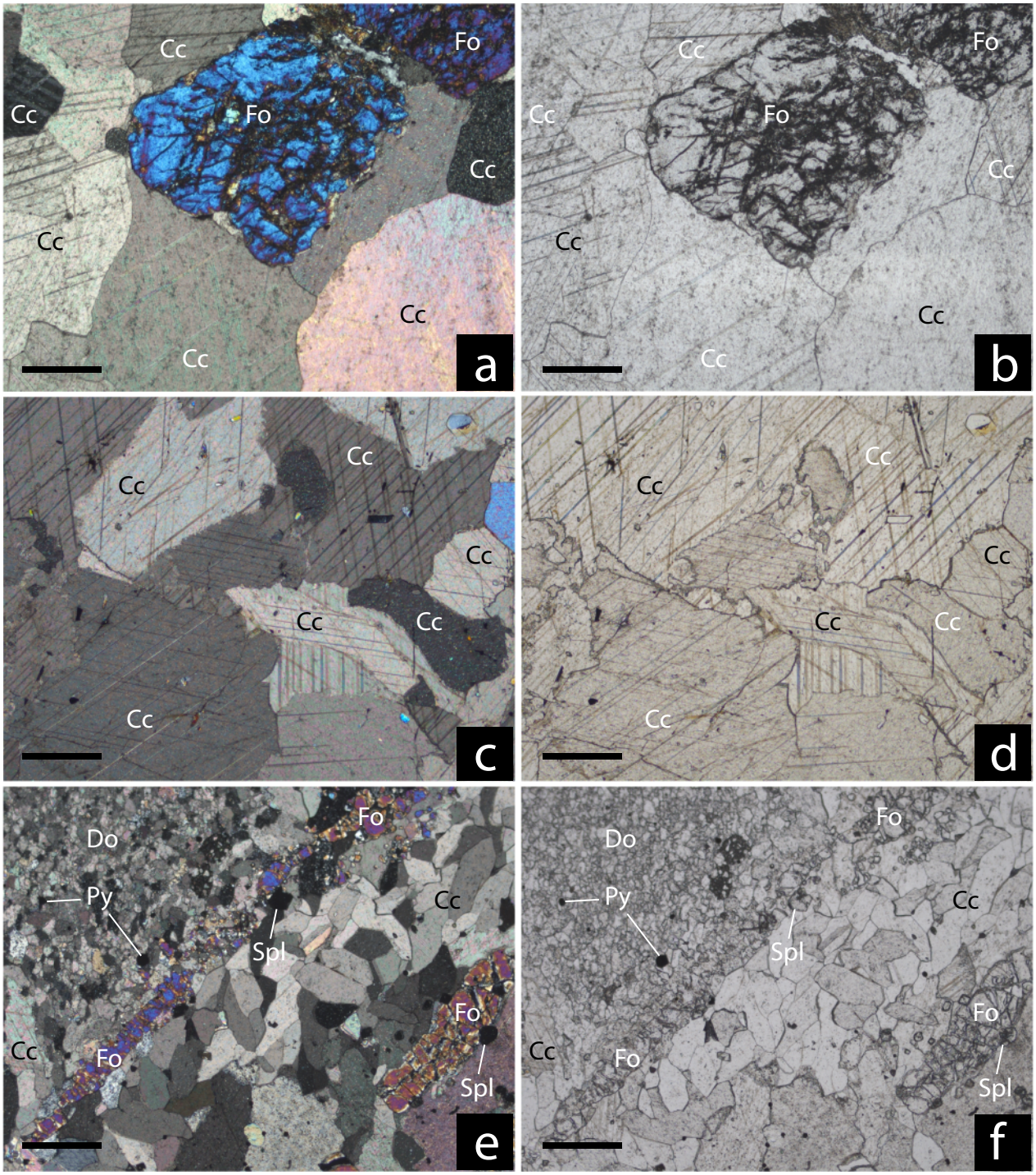

Figure S3. Photomicrographs of dolomite from the Alta stock inner aureole. a–b) Sample AS17-74, at the contact with the Alta stock: very coarse-grained calcite (Cc) and forsterite (Fo) crystals in cross polarized (a) and planar (b) light. c–d) Sample AS17-37b, 0.4 km from the Alta stock: coarse-grained Cc in cross polarized (c) and planar (d) light. e–f) Sample AS17-73, 0.5 km from the Alta stock: coarse-grained Cc vein with forsterite (Fo) in fine-grained dolomite (Do) country rock and minor pyrite (Py) and spinel (Spl) in cross polarized (e) and planar (f) light. Scale bar is 500 μm.

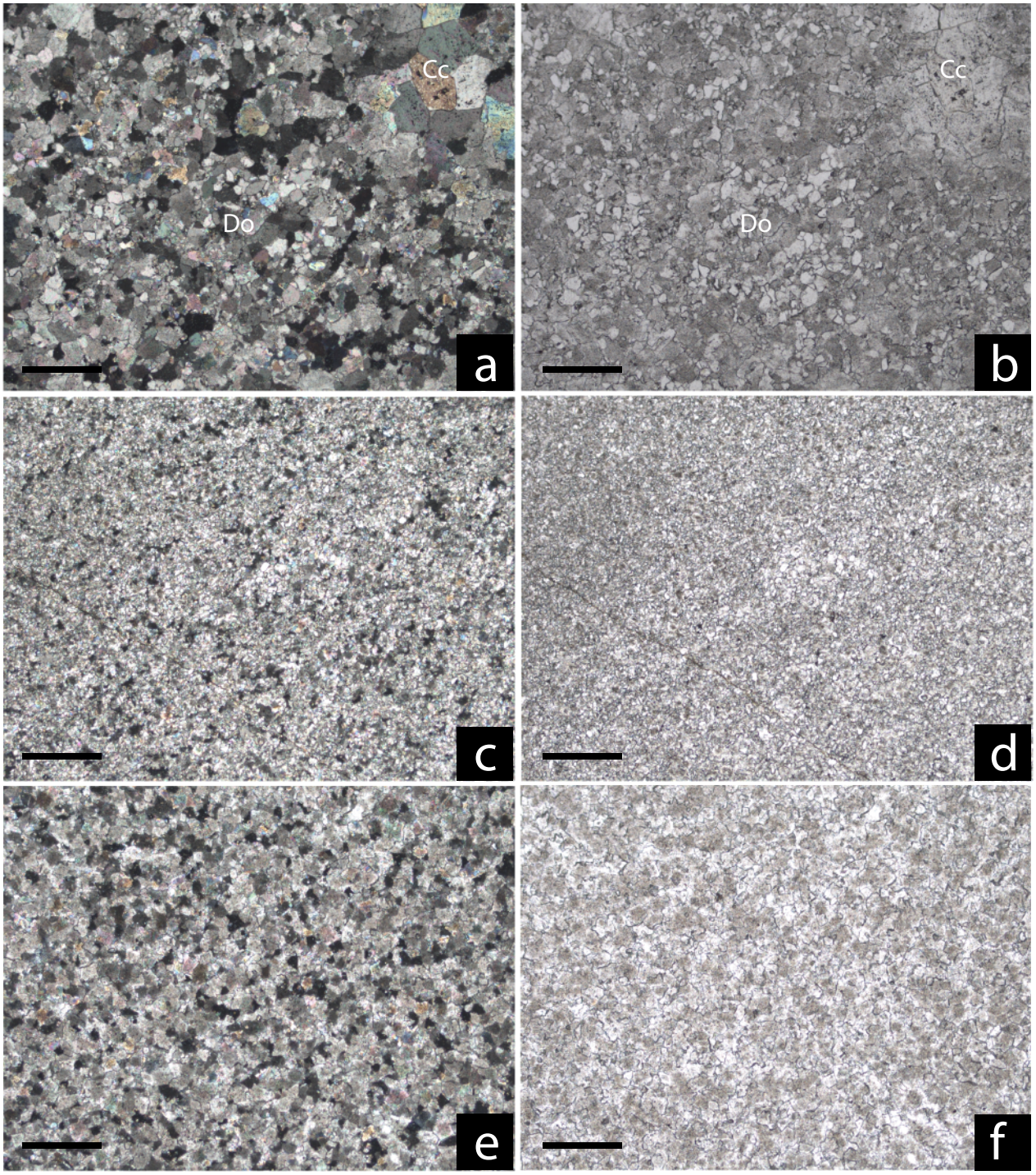

Figure S4. Photomicrographs of dolomite from the Alta stock outer aureole. a–b) Sample AS17-39, 0.7 km from the Alta stock: coarse-grained calcite (Cc) vein in finer-grained dolomite (Do) country rock in cross polarized (a) and planar (b) light. c–d) Sample AS17-70, 1.0 km from the Alta stock: very fine-grained Do in cross polarized (c) and planar (d) light. e–f) Sample AS17-26, 1.6 km from the Alta stock: fine-grained dolomite (Do) in cross polarized (e) and planar (f) light. Scale bar is 500 μm.

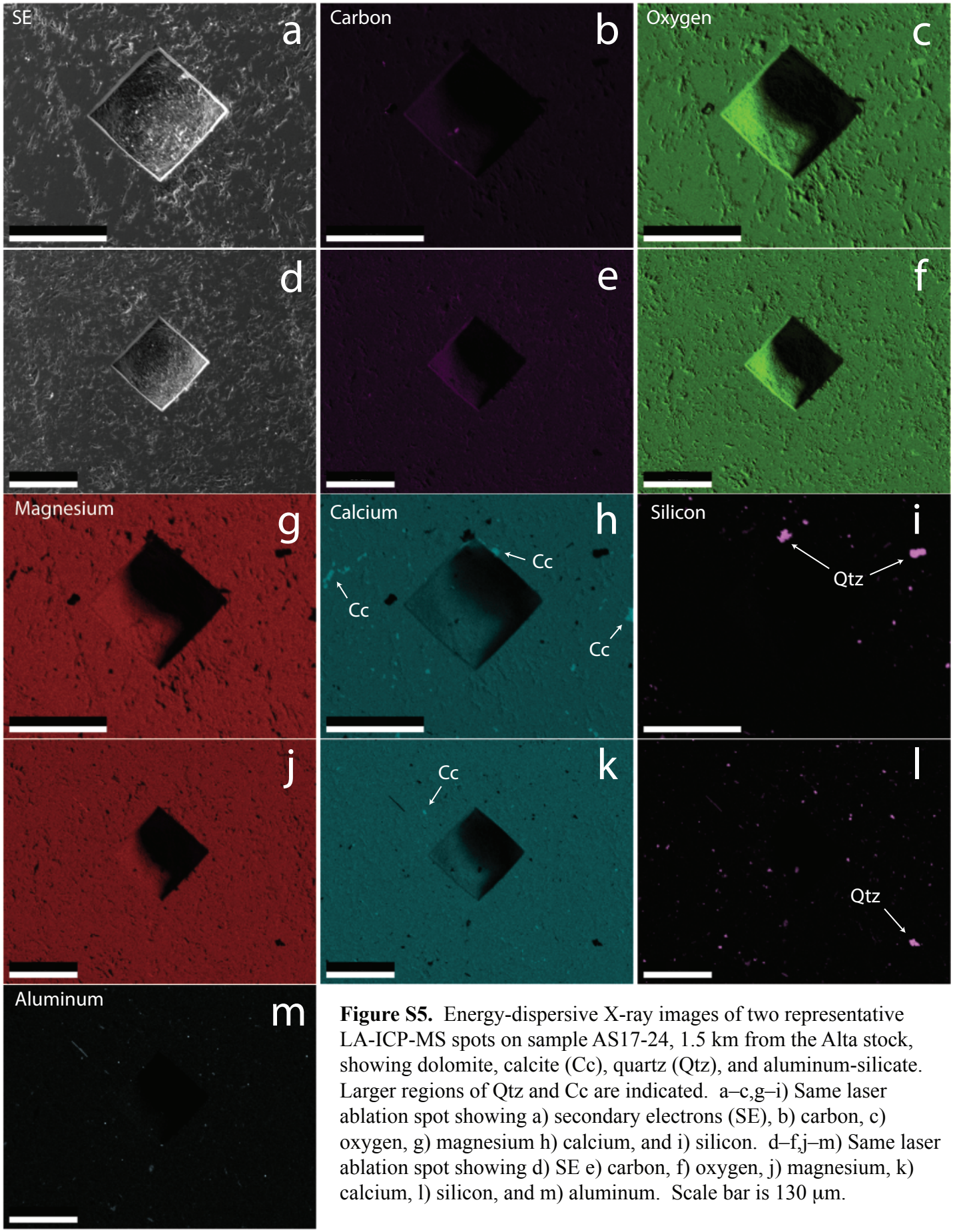

Figure S5. Energy-dispersive X-ray images of two representative LA-ICP-MS spots on sample AS17-24, 1.5 km from the Alta stock, showing dolomite, calcite (Cc), quartz (Qtz), and aluminum-silicate. Larger regions of Qtz and Cc are indicated. a–c,g–i) Same laser ablation spot showing a) secondary electrons (SE), b) carbon, c) oxygen, g) magnesium h) calcium, and i) silicon. d–f,j–m) Same laser ablation spot showing d) SE e) carbon, f) oxygen, j) magnesium, k) calcium, l) silicon, and m) aluminum. Scale bar is 130 μm.

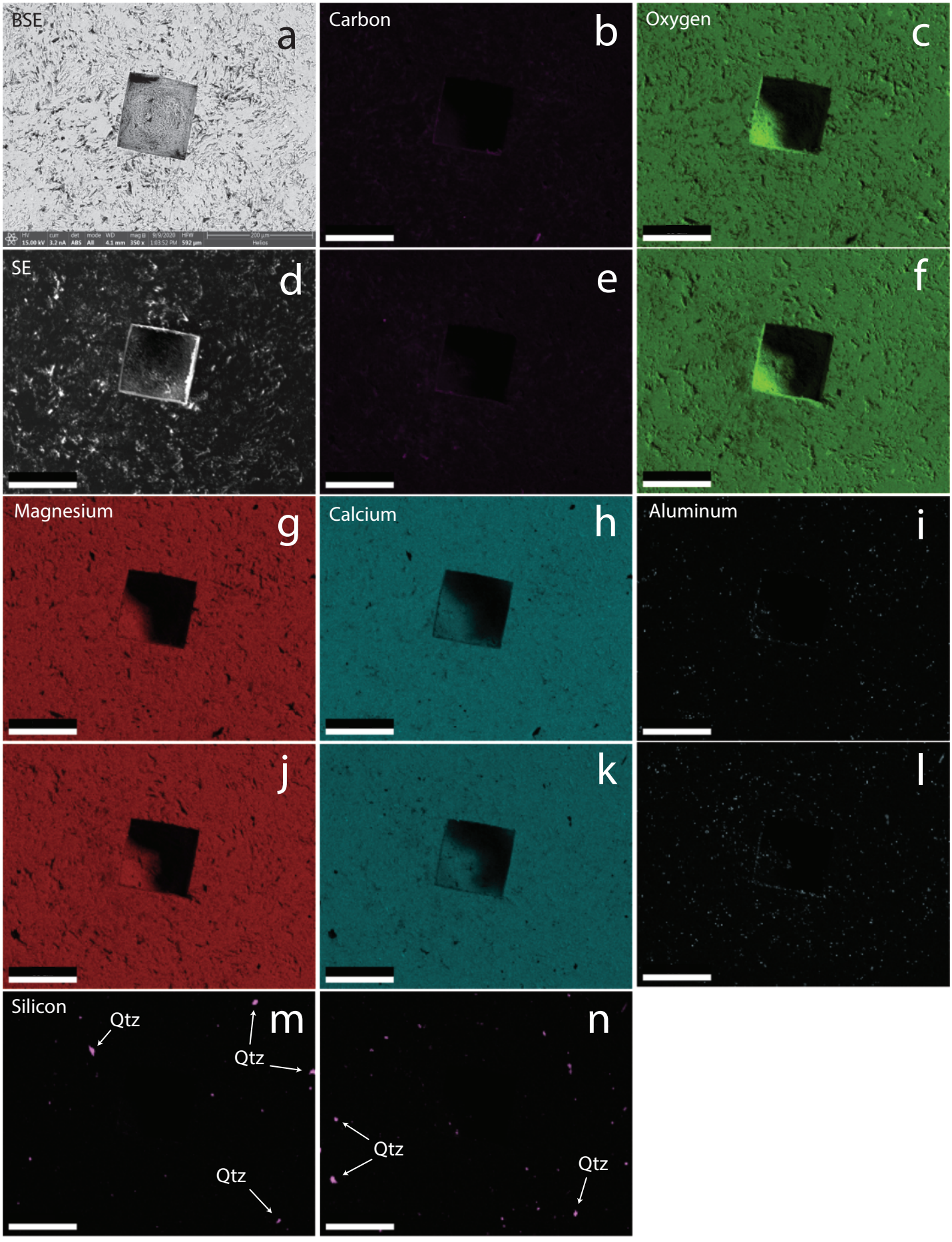
BSE
a
Carbon
b
Oxygen
c
SE
d
e
f
Magnesium
g
Calcium
h
Aluminum
i
j
k
l
Silicon
Qtz
Qtz
m
Qtz
Qtz
n
Qtz

Figure S6. Energy-dispersive X-ray images of two representative LA-ICP-MS spots on sample AS17-26, 1.6 km from the Alta stock, showing dolomite and quartz (Qtz). Larger regions of Qtz are indicated. a–c,g–i,m) Single laser ablation spot showing a) back-scattered electrons (BSE), b) carbon, c) oxygen, g) magnesium, h) calcium, i) aluminum, and l) silicon. d–f,j–l,n) Single laser ablation spot showing d) secondary electrons (SE) e) carbon, f) oxygen, j) magnesium, k) calcium, l) aluminum, and n) silicon. Scale bar is 130 μm.

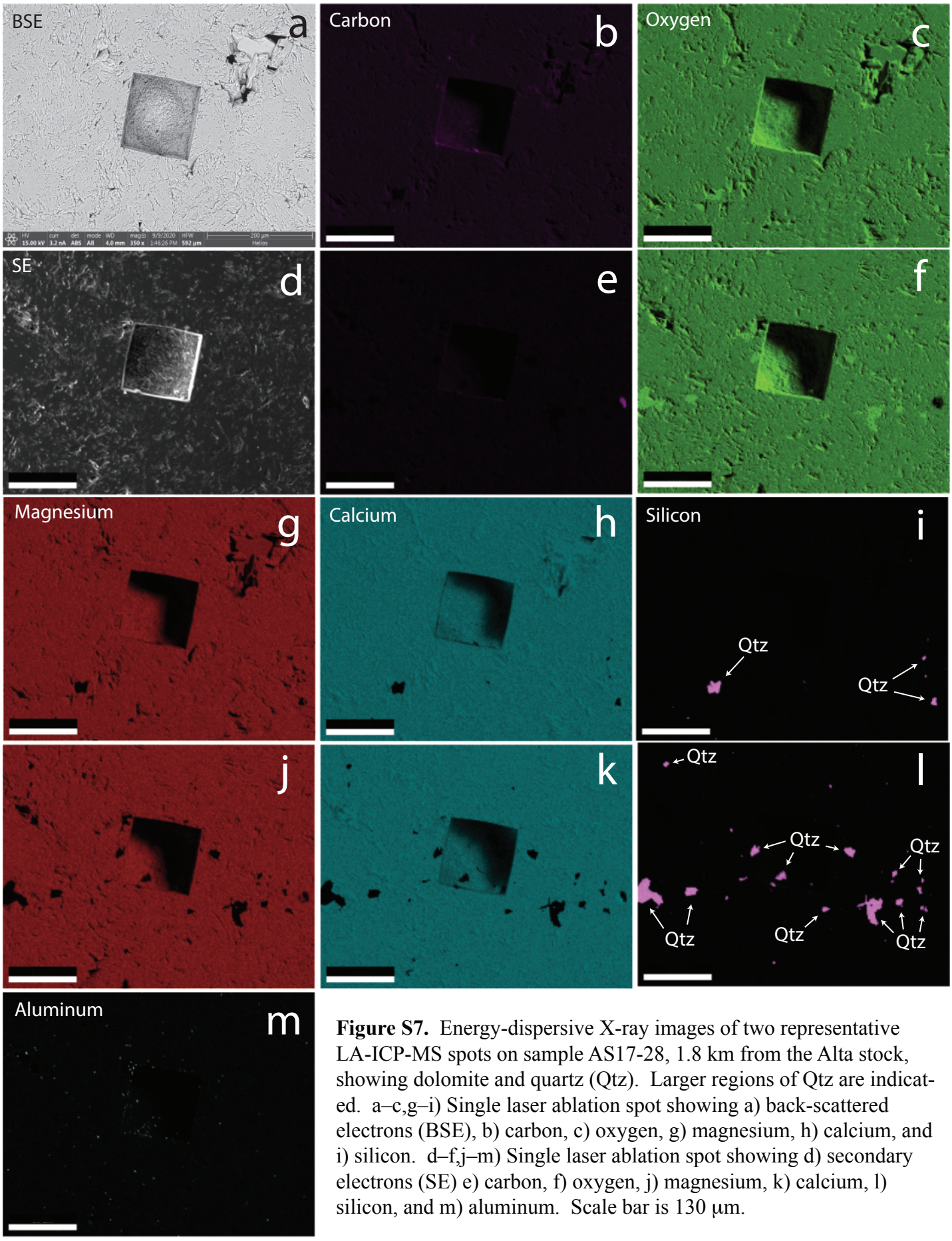

Figure S7. Energy-dispersive X-ray images of two representative LA-ICP-MS spots on sample AS17-28, 1.8 km from the Alta stock, showing dolomite and quartz (Qtz). Larger regions of Qtz are indicated. a–c,g–i) Single laser ablation spot showing a) back-scattered electrons (BSE), b) carbon, c) oxygen, g) magnesium, h) calcium, and i) silicon. d–f,j–m) Single laser ablation spot showing d) secondary electrons (SE) e) carbon, f) oxygen, j) magnesium, k) calcium, l) silicon, and m) aluminum. Scale bar is 130 μm.

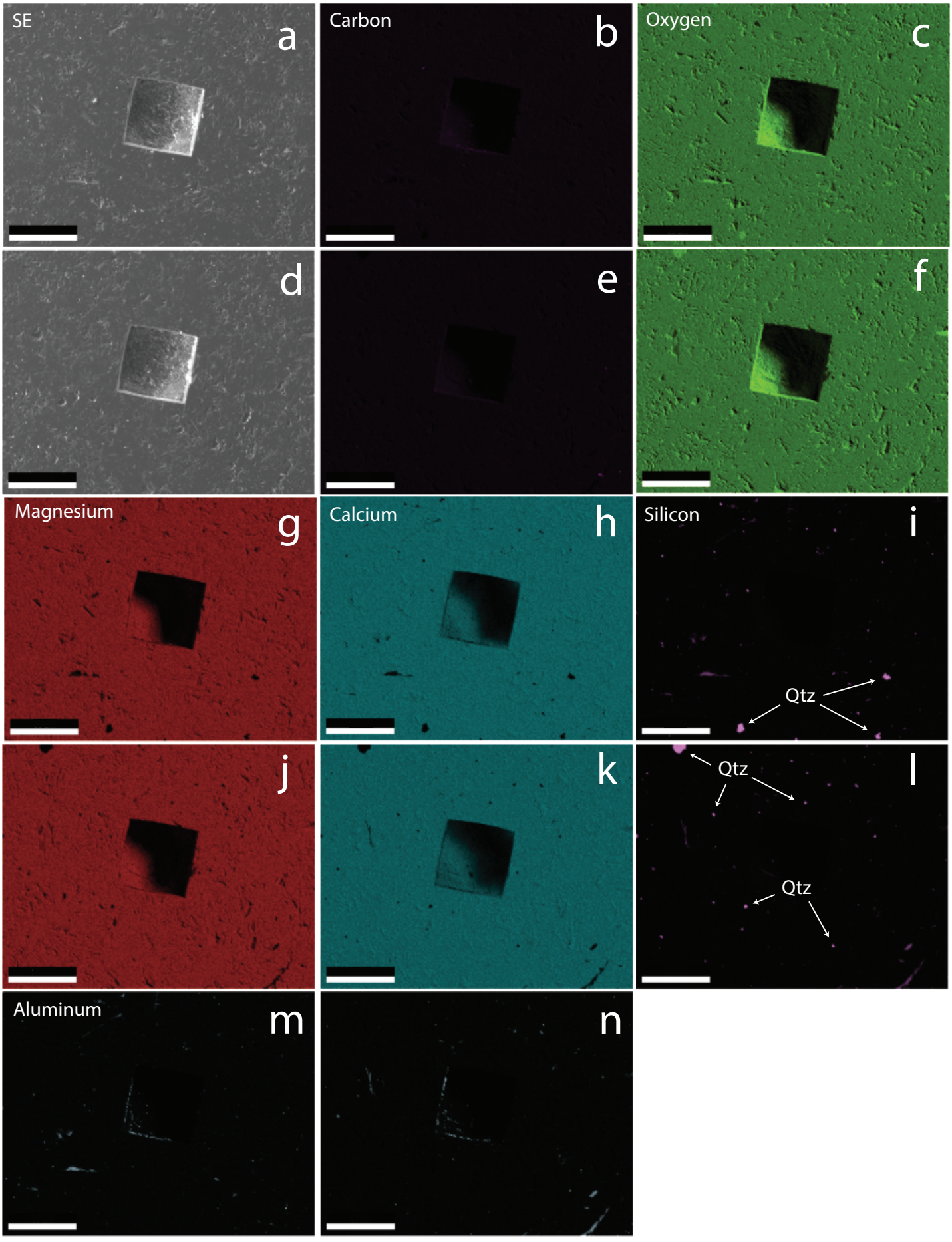
SE
a
Carbon
b
Oxygen
c
d
e
f
Magnesium
g
Calcium
h
Silicon
i
Qtz
j
k
Qtz
Qtz
l
Aluminum
m
n

Figure S8. Energy-dispersive X-ray images of two representative LA-ICP-MS spots on sample AS17-29, 2.0 km from the Alta stock, showing dolomite and quartz (Qtz). a–c,g–i,m) Single laser ablation spot showing a) secondary electrons (SE), b) carbon, c) oxygen, g) magnesium, h) calcium, i) silicon, and m) aluminum. d–f,j–l,n) Single laser ablation spot showing d) SE e) carbon, f) oxygen, j) magnesium, k) calcium, l) silicon, and n) aluminum. Scale bar is 130 μm.

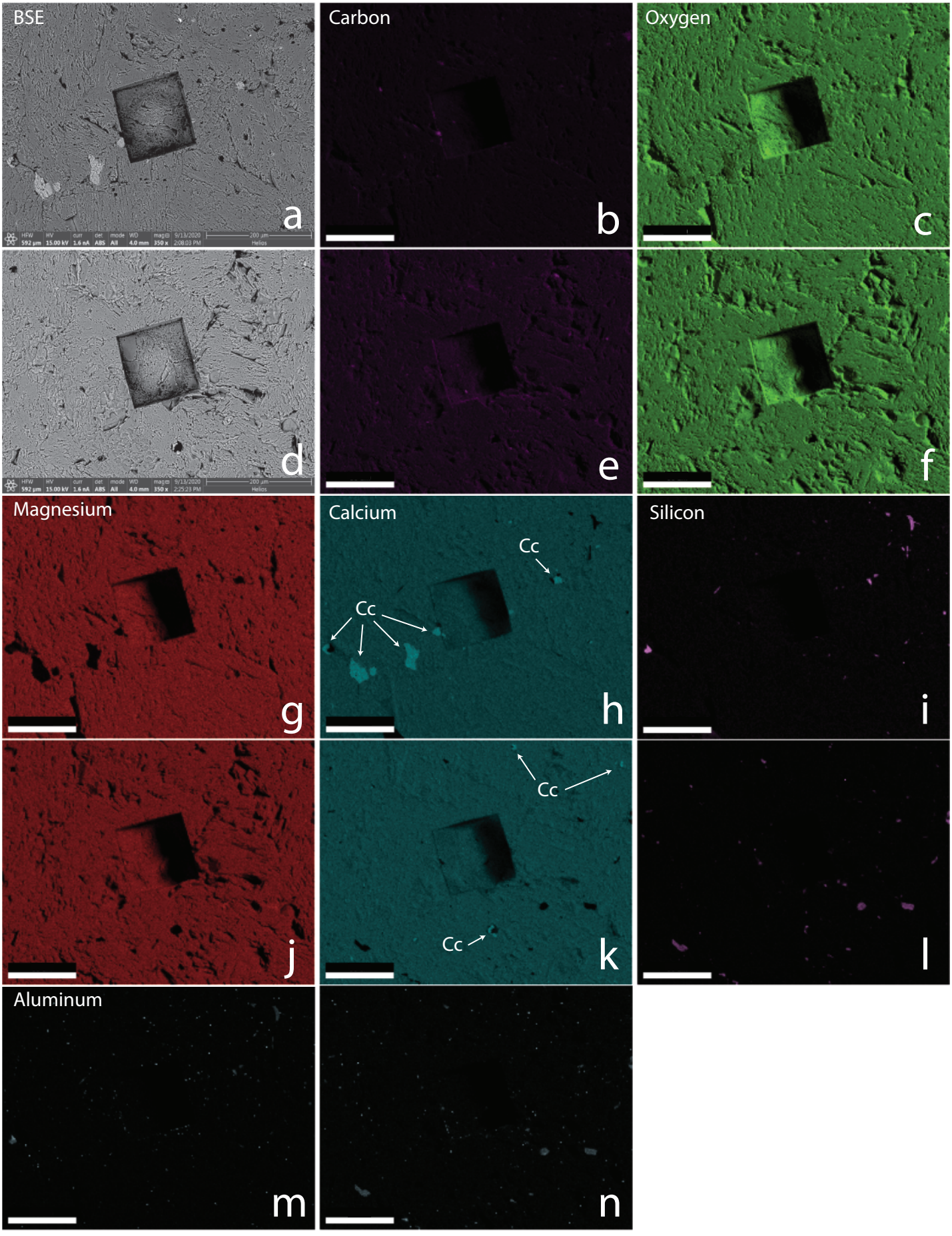
BSE
a
Carbon
b
Oxygen
c
d
e
f
Magnesium
g
Calcium
Cc
Cc
h
Silicon
i
j
Cc
Cc
k
l
Aluminum
m
n

Figure S9. Energy-dispersive X-ray images of two representative LA-ICP-MS spots on sample AS17-39, 0.7 km from the Alta stock, showing dolomite, calcite (Cc), and aluminum-silicate. a–c,g–i,m) Same laser ablation spot showing a) back-scattered electrons (BSE), b) carbon, c) oxygen, g) magnesium h) calcium, i) silicon, and m) aluminum. d–f,j–l,n) Same laser ablation spot showing d) BSE e) carbon, f) oxygen, j) magnesium, k) calcium, l) silicon, and n) aluminum. Scale bar is 130 μm.

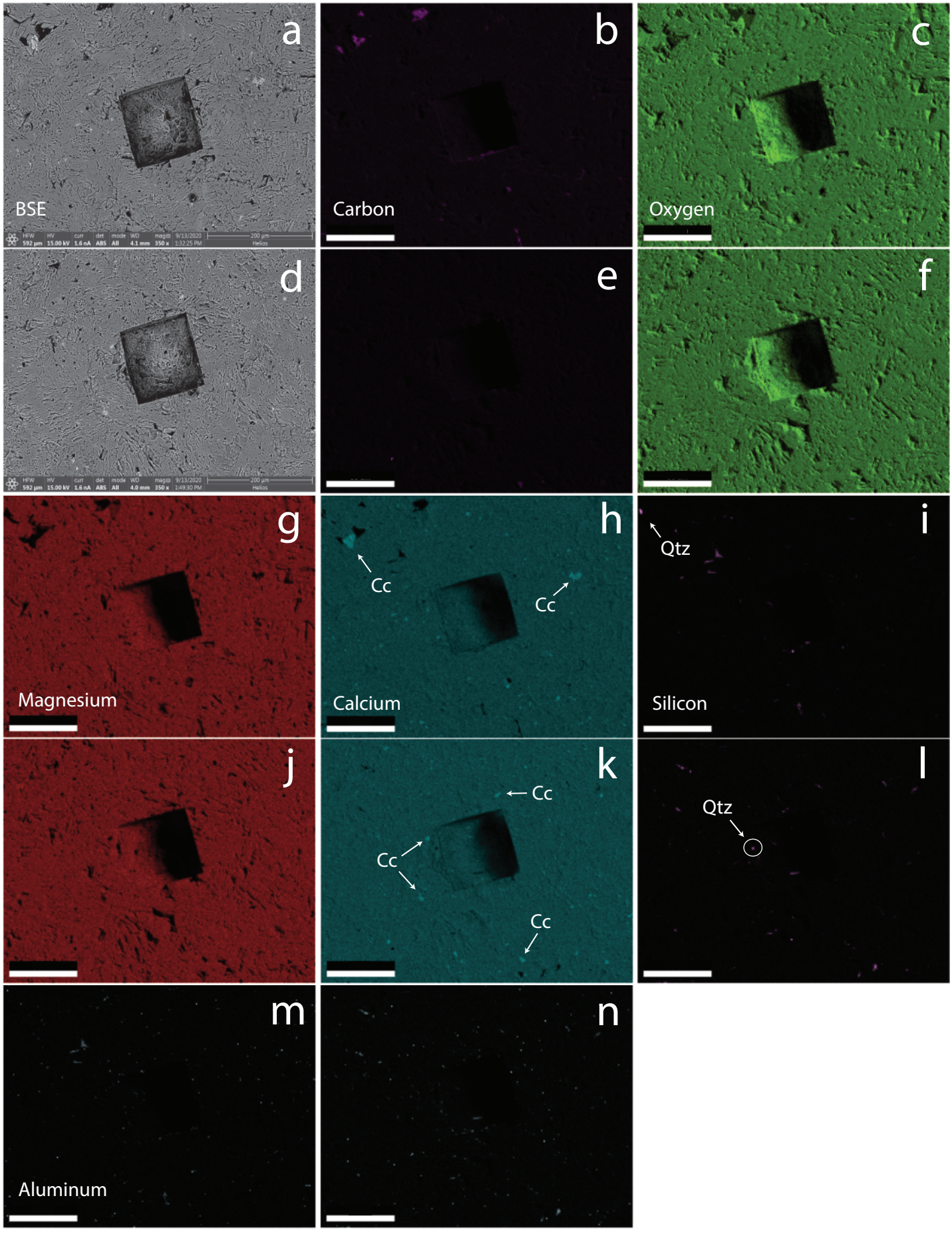
a
BSE
b
Carbon
c
Oxygen
d
e
f
g
Magnesium
h
Cc
Cc
Calcium
i
Qtz
Silicon
j
k
Cc
Cc
Cc
l
Qtz
m
Aluminum
n

Figure S10. Energy-dispersive X-ray images of two representative LA-ICP-MS spots on sample AS17-44, 1.2 km from the Alta stock, showing dolomite calcite (Cc), and quartz (Qtz). a–c,g–i,m) Same laser ablation spot showing a) back-scattered electrons (BSE), b) carbon, c) oxygen, g) magnesium h) calcium, i) silicon, and m) aluminum. d–f,j–l,n) Same laser ablation spot showing d) BSE e) carbon, f) oxygen, j) magnesium, k) calcium, l) silicon, and n) aluminum. Scale bar is 130 μm.

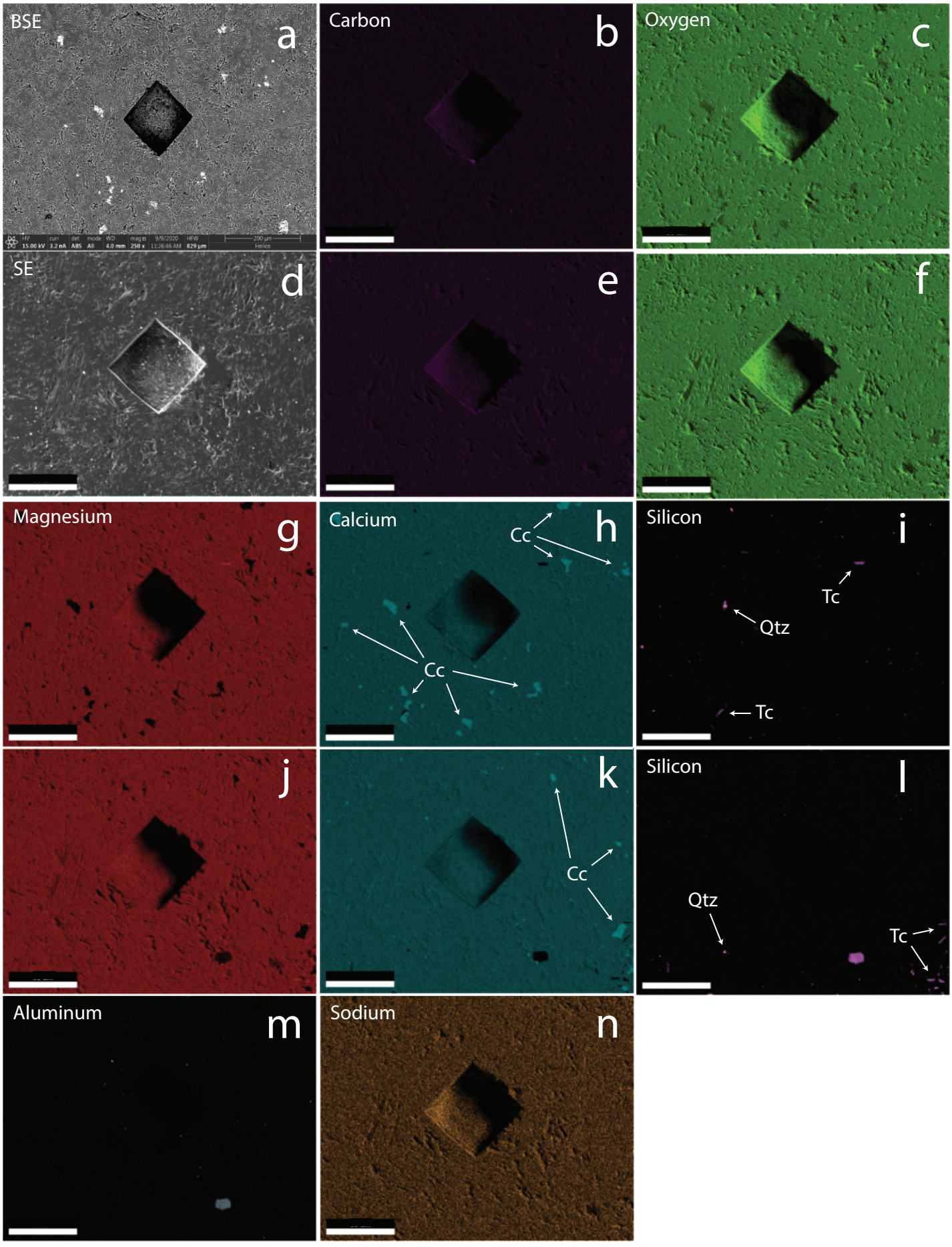
BSE
a
Carbon
b
Oxygen
c
SE
d
e
f
Magnesium
g
Calcium
Cc
h
Cc
Silicon
i
Tc
Qtz
Tc
j
k
Cc
Silicon
l
Qtz
Tc
Aluminum
m
Sodium
n

Figure S11. Energy-dispersive X-ray images of two representative LA-ICP-MS spots on sample AS17-68g, 1.4 km from the Alta stock, showing dolomite, calcite (Cc), talc (Tc), quartz (Qtz) and aluminum-silicate. a–c,g–i) Single laser ablation spot showing a) back-scattered electrons (BSE), b) carbon, c) oxygen, g) magnesium, h) calcium, and i) silicon. d–f,j–n) Single laser ablation spot showing d) secondary electrons (SE) e) carbon, f) oxygen, j) magnesium, k) calcium, l) silicon, m) aluminum, and n) sodium. Scale bar is 130 μm.

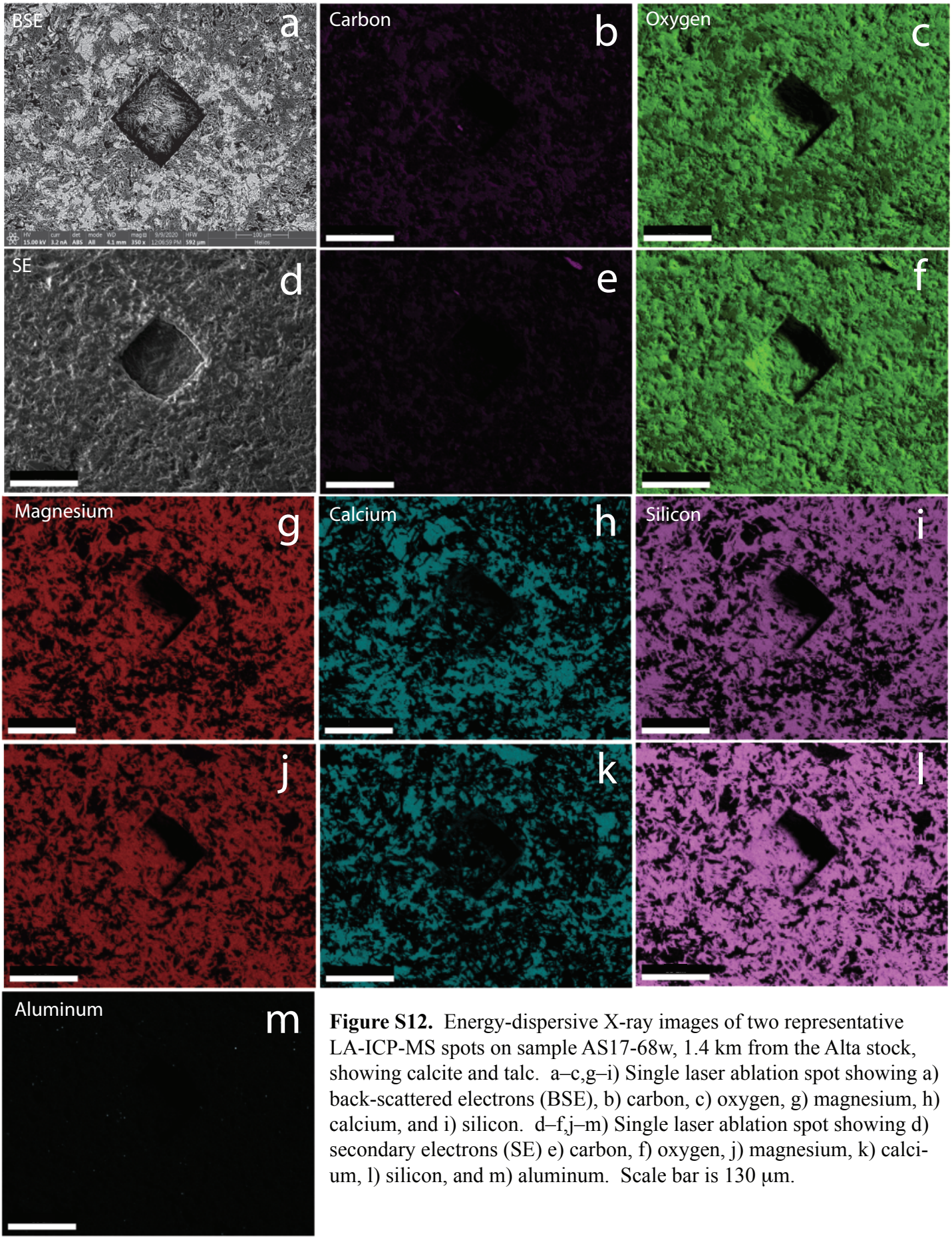

Figure S12. Energy-dispersive X-ray images of two representative LA-ICP-MS spots on sample AS17-68w, 1.4 km from the Alta stock, showing calcite and talc. a–c,g–i) Single laser ablation spot showing a) back-scattered electrons (BSE), b) carbon, c) oxygen, g) magnesium, h) calcium, and i) silicon. d–f,j–m) Single laser ablation spot showing d) secondary electrons (SE) e) carbon, f) oxygen, j) magnesium, k) calcium, l) silicon, and m) aluminum. Scale bar is 130 μm.

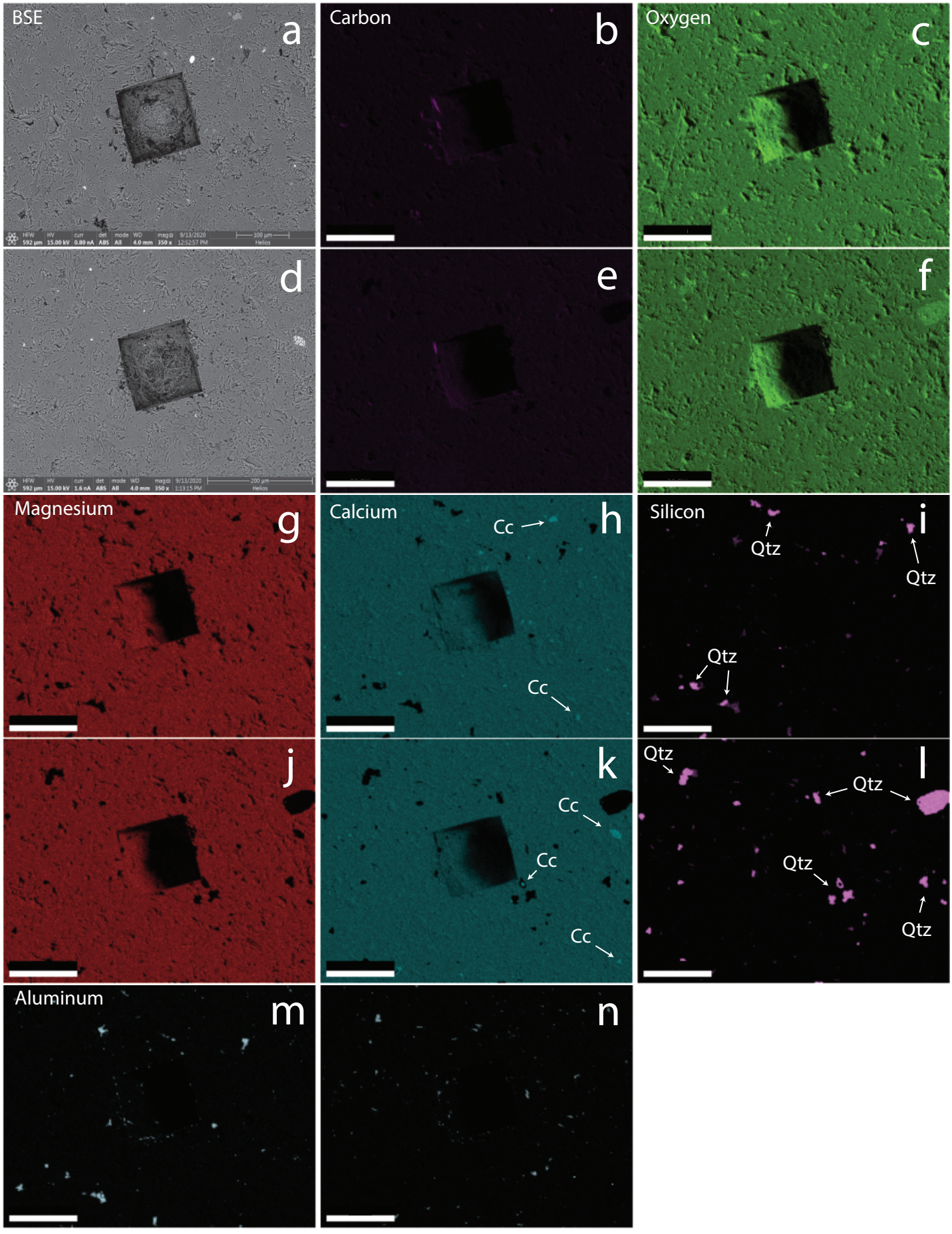
BSE
a
Carbon
b
Oxygen
c
d
e
f
Magnesium
g
Calcium
Cc
h
Cc
Silicon
Qtz
i
Qtz
Qtz
j
k
Cc
Cc
Cc
Qtz
l
Qtz
Qtz
Qtz
Aluminum
m
n

Figure S13. Energy-dispersive X-ray images of two representative LA-ICP-MS spots on sample AS17-70, 1.0 km from the Alta stock, showing dolomite, calcite (Cc), quartz (Qtz), and aluminum-silicate. Larger regions of Cc and Qtz indicated. a–c,g–i,m) Same laser ablation spot showing a) back-scattered electrons (BSE), b) carbon, c) oxygen, g) magnesium h) calcium, i) silicon, and m) aluminum. d–f,j–l,n) Same laser ablation spot showing d) BSE e) carbon, f) oxygen, j) magnesium, k) calcium, l) silicon, and n) aluminum. Scale bar is 130 μm.

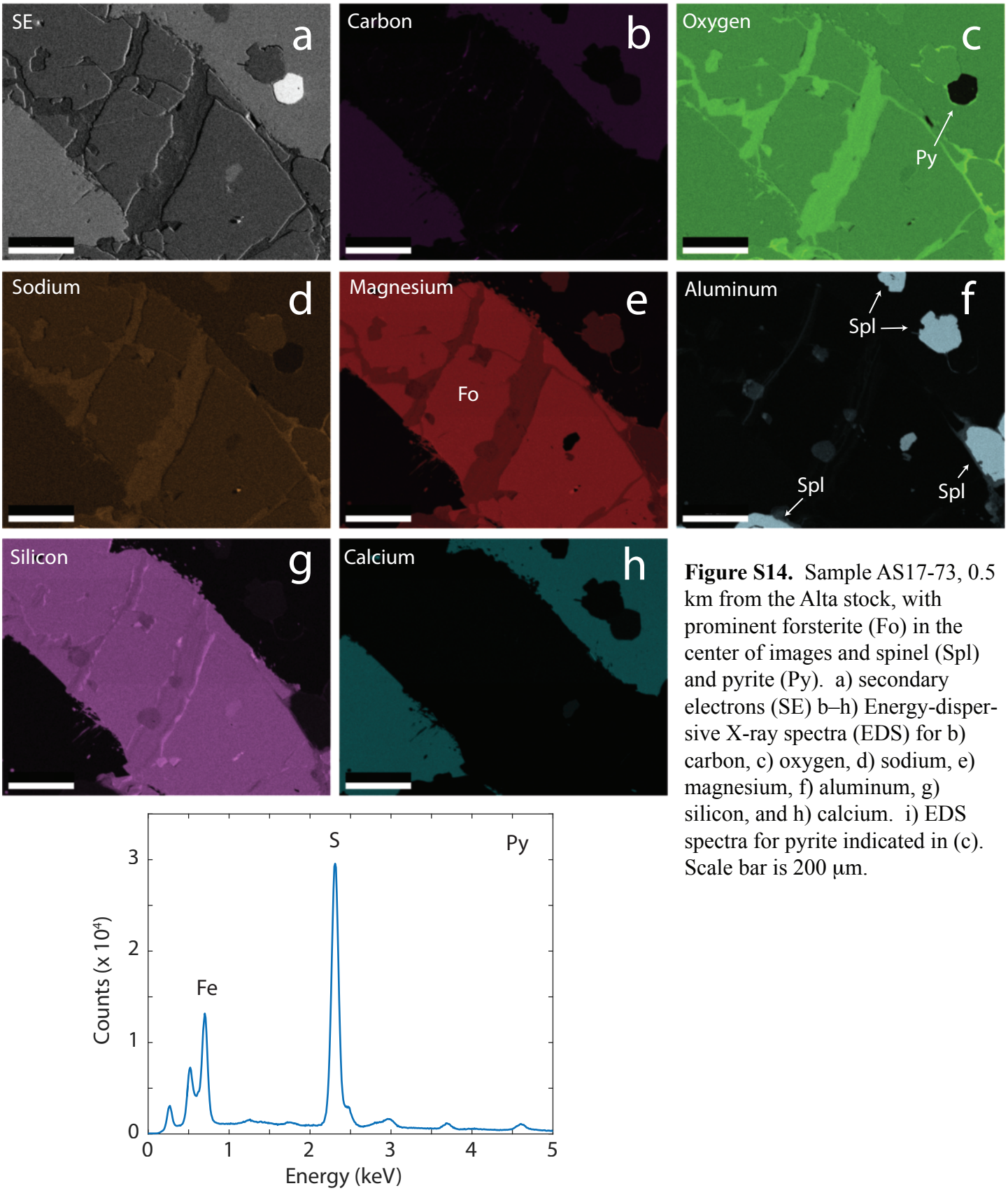

Figure S14. Sample AS17-73, 0.5 km from the Alta stock, with prominent forsterite (Fo) in the center of images and spinel (Spl) and pyrite (Py). a) secondary electrons (SE) b–h) Energy-dispersive X-ray spectra (EDS) for b) carbon, c) oxygen, d) sodium, e) magnesium, f) aluminum, g) silicon, and h) calcium. i) EDS spectra for pyrite indicated in (c). Scale bar is 200 μm.

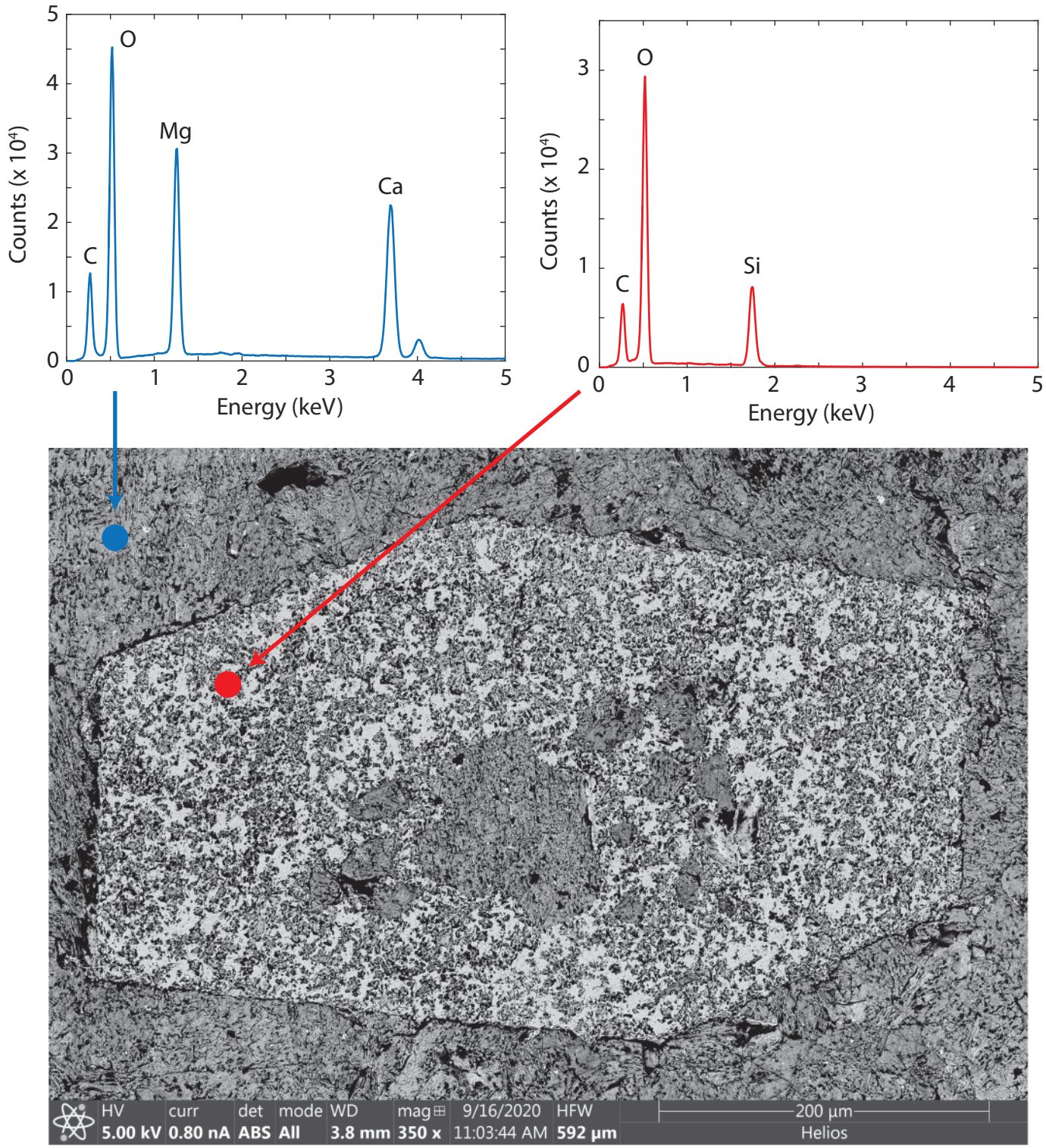

Figure S15. Energy-dispersive X-ray spectra (EDS) and back-scattered electron (BSE) image of AS17-44, 1.2 km from the Alta stock, within 500 µm of multiple LA-ICP-MS spots. a) EDS of dolomite matrix. b) EDS of quartz. c) BSE image. Scale bar is 200 µm.

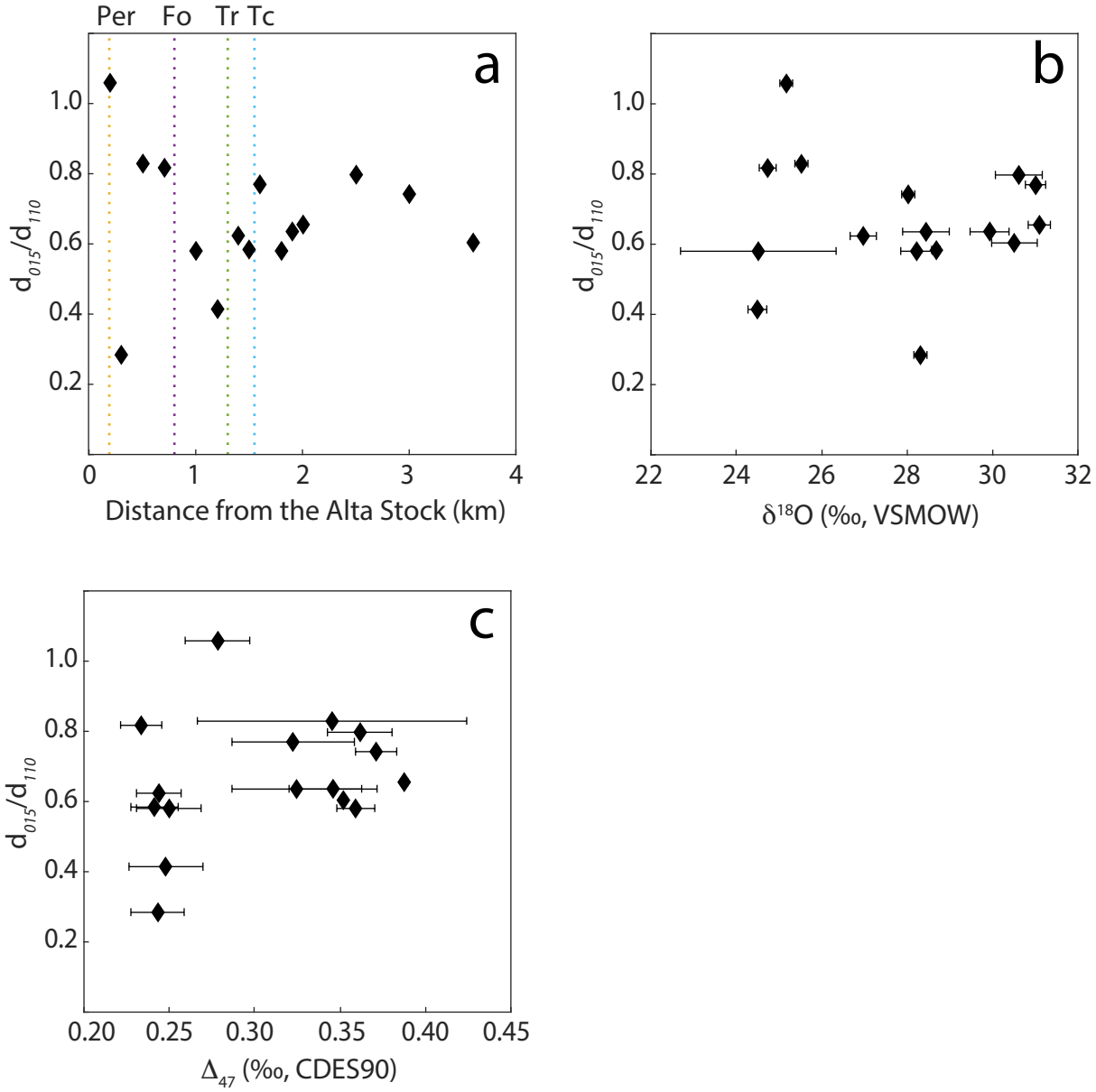

Figure S16. a) Cation ordering in dolomite plotted as a function of a) distance from the Alta stock, b) Δ_{47} values, and c) $\delta^{18}O$ values. Black diamonds represent cation ordering for dolomite samples and is estimated from the intensity ratio of d_{015}/d_{110}. Vertical dashed lines indicate the approximate location of isograds: yellow is periclase (Per), purple is forsterite (Fo), green is tremolite (Tr), and cyan is talc (Tc). c) Cation ordering in dolomite plotted as a function of $\delta^{18}O$ values. Error bars in (b) and (c) represent 95% C.I. for replicate analyses or are smaller than symbol size if absent.

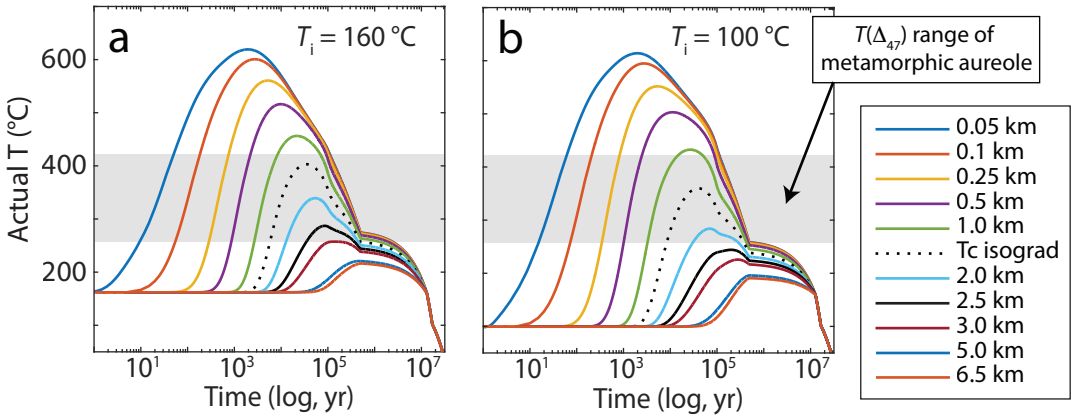

Figure S17. a) Actual temperature as a function of time (logarithmic scale) after emplacement of the Alta stock using the exhumation history of Armstrong et al. (2003) and initial temperature (T_i) for the sampling transect of 160 °C and maximum temperature (T_{max}) at the talc (Tc) isograd of 400 °C. Curves represent distances from the Alta stock of 0.05–6.5 km. The dashed black curve represents the talc isograd. The grey region represents the $T(\Delta_{47})$ range within the metamorphic aureole. b) same as (a) but T_i = 100 °C and Tc isograd T_{max} = 350 °C.

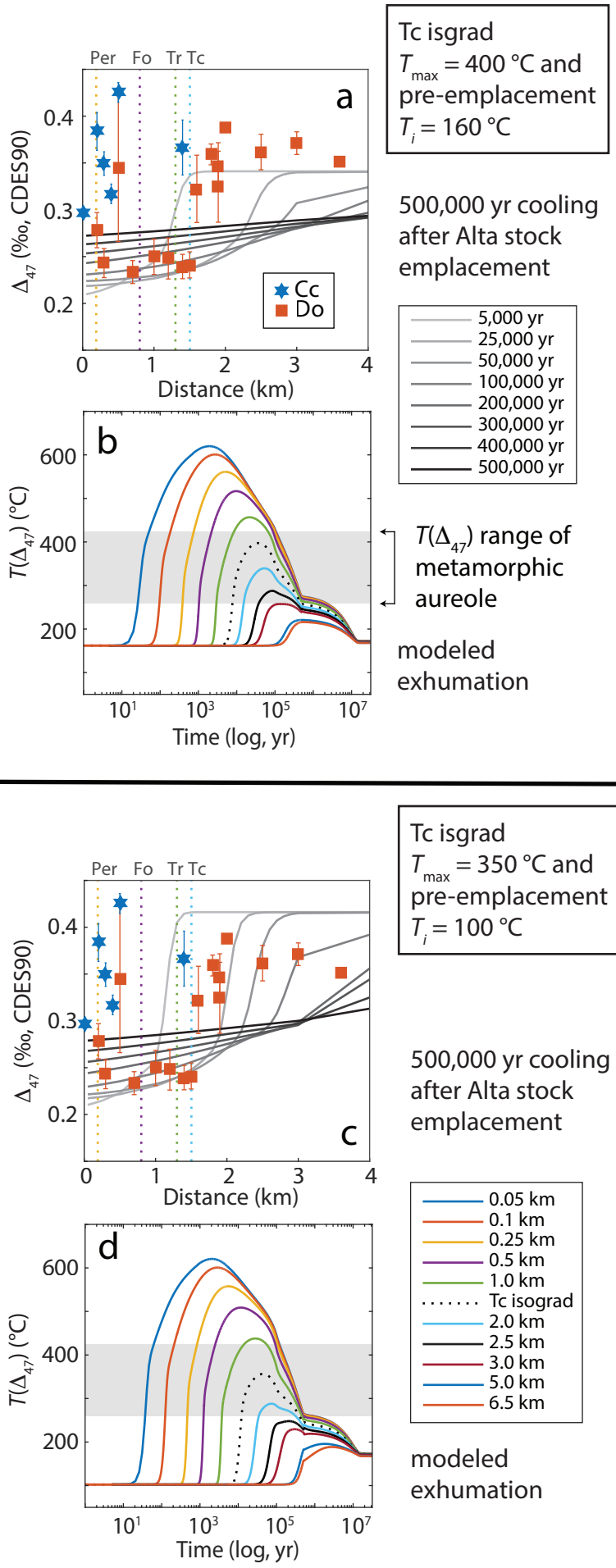

Figure S18. a) Measured dolomite Δ_{47} values, plotted as a function of distance from the Alta stock (symbols), compared to modeled Δ_{47} values (curves) 5–500 kyr after stock emplacement with sampling transect initial temperature (T_i) of 160 °C and talc (Tc) isograd peak temperature (T_{max}) of 400 °C, using the disordered model and kinetic parameters of Hemingway and Henkes (2020). Symbols represent replicate averages. Error bars represent 95% C.I. for replicate analyses or are smaller than symbol size if absent. Vertical dashed lines indicate the approximate location of isograds: Per is periclase, Fo is forsterite, and Tr is tremolite. b) Modeled $T(\Delta_{47})$ as a function of time (logarithmic scale) after emplacement of the Alta stock using the exhumation history of Armstrong et al. (2003). Curves represent distances from the Alta stock of 0.05–6.5 km. The dashed black curve represents the talc isograd. Grey region represents $T(\Delta_{47})$ range of the metamorphic aureole. c–d) Same as (a–b) except T_i = 100 °C and Tc isograd T_{max} = 350 °C. See supporting information S2 for modeling specifics.

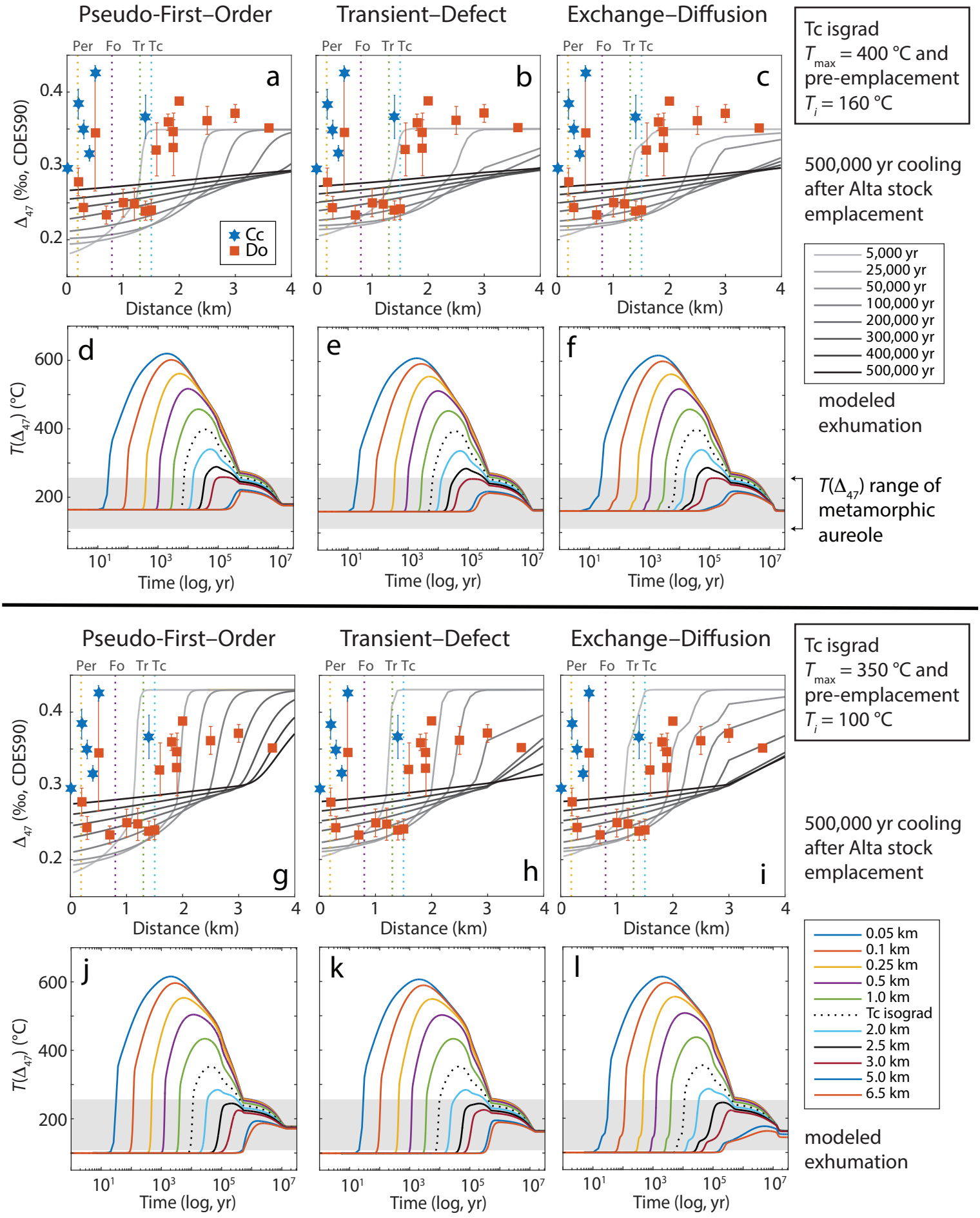

Figure S19. Same as Fig. 6 in main text except for calcite.

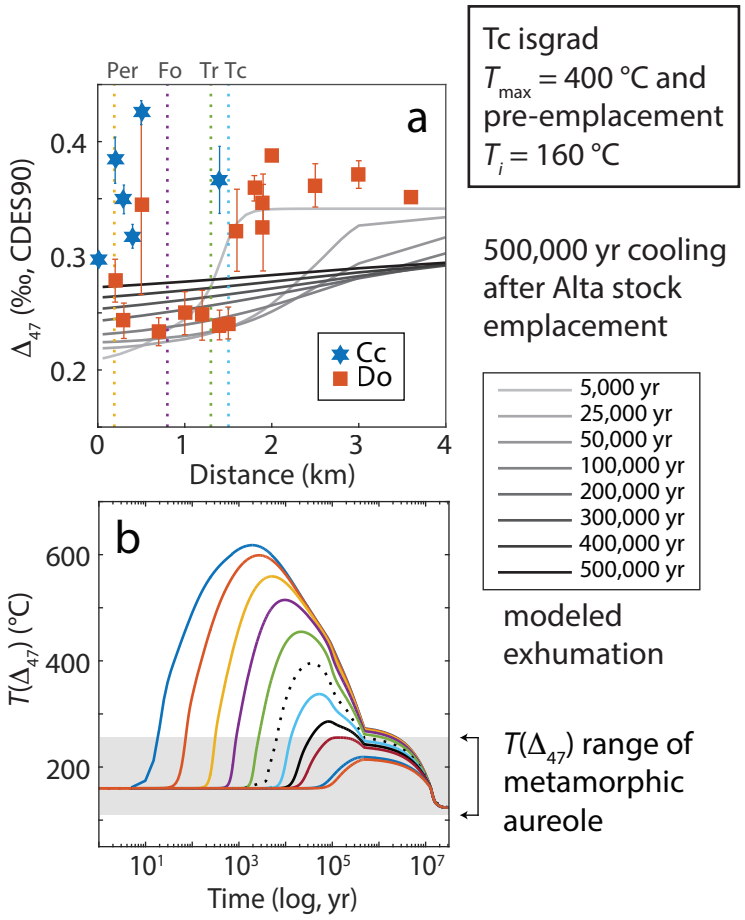

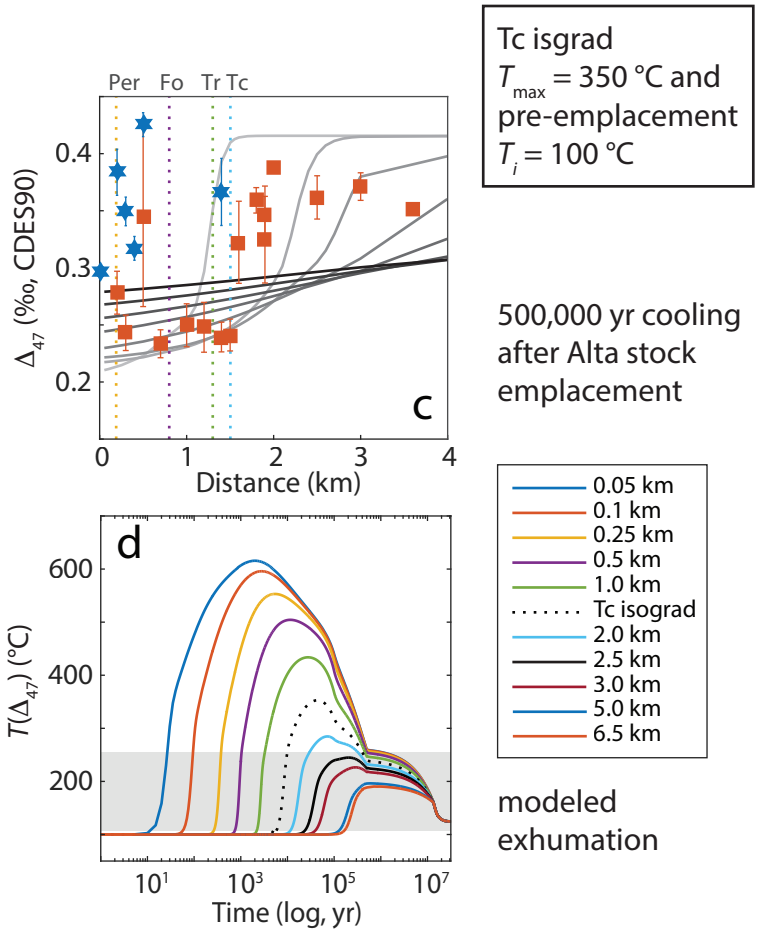

Figure S20. a) Measured calcite Δ_{47} values, plotted as a function of distance from the Alta stock (symbols), compared to modeled Δ_{47} values (curves) 5–500 kyr after stock emplacement with sampling transect initial temperature (T_i) of 160 °C and talc (Tc) isograd peak temperature (T_{max}) of 400 °C, using the disordered model and kinetic parameters of Hemingway and Henkes (2020). Symbols represent replicate averages. Error bars represent 95% C.I. for replicate analyses or are smaller than symbol size if absent. Vertical dashed lines indicate the approximate location of isograds: Per is periclase, Fo is forsterite, and Tr is tremolite. b) Modeled $T(\Delta_{47})$ as a function of time (logarithmic scale) after emplacement of the Alta stock using the exhumation history of Armstrong et al. (2003). Curves represent distances from the Alta stock of 0.05–6.5 km. The dashed black curve represents the talc isograd. Grey region represents $T(\Delta_{47})$ range of the metamorphic aureole. c–d) Same as (a–b) except T_i = 100 °C and Tc isograd T_{max} = 350 °C. See supporting information S2 for modeling specifics.

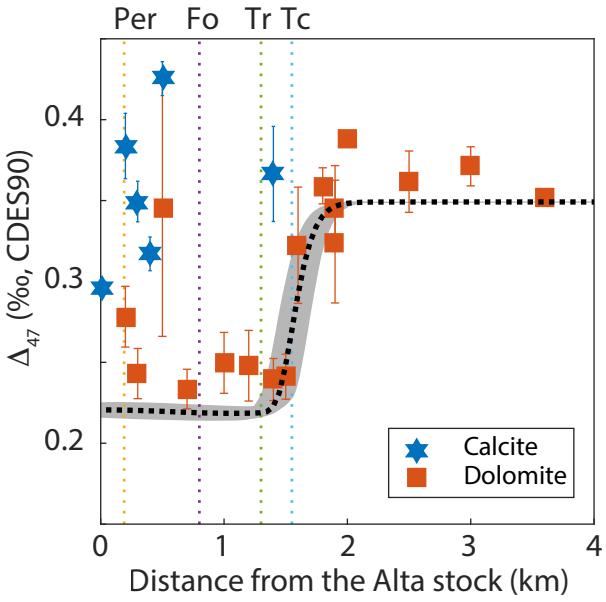

Figure S21. Modeled Monte Carlo simulation results for dolomite clumped isotope reordering kinetic parameters and calcite and dolomite Δ_{47} values for samples plotted as a function of distance from the Alta stock. Symbols represent replicate averages: red squares are dolomite and blue stars are calcite. Error bars represent the 95% C.I. for replicate analyses or are smaller than symbol size if absent. Vertical dashed lines indicate the location of isograds: yellow is periclase (Per), purple is forsterite (Fo), green is tremolite (Tr), and cyan is talc (Tc). Thick dashed curve represents average sigmoidal profile of modeled Δ_{47} values after a cooling duration of 100 ky based on kinetic parameters for dolomite from Monte Carlo simulations. Grey region represents the full range of possible modeled Δ_{47} values based on kinetic parameters for dolomite from Monte Carlo simulations.

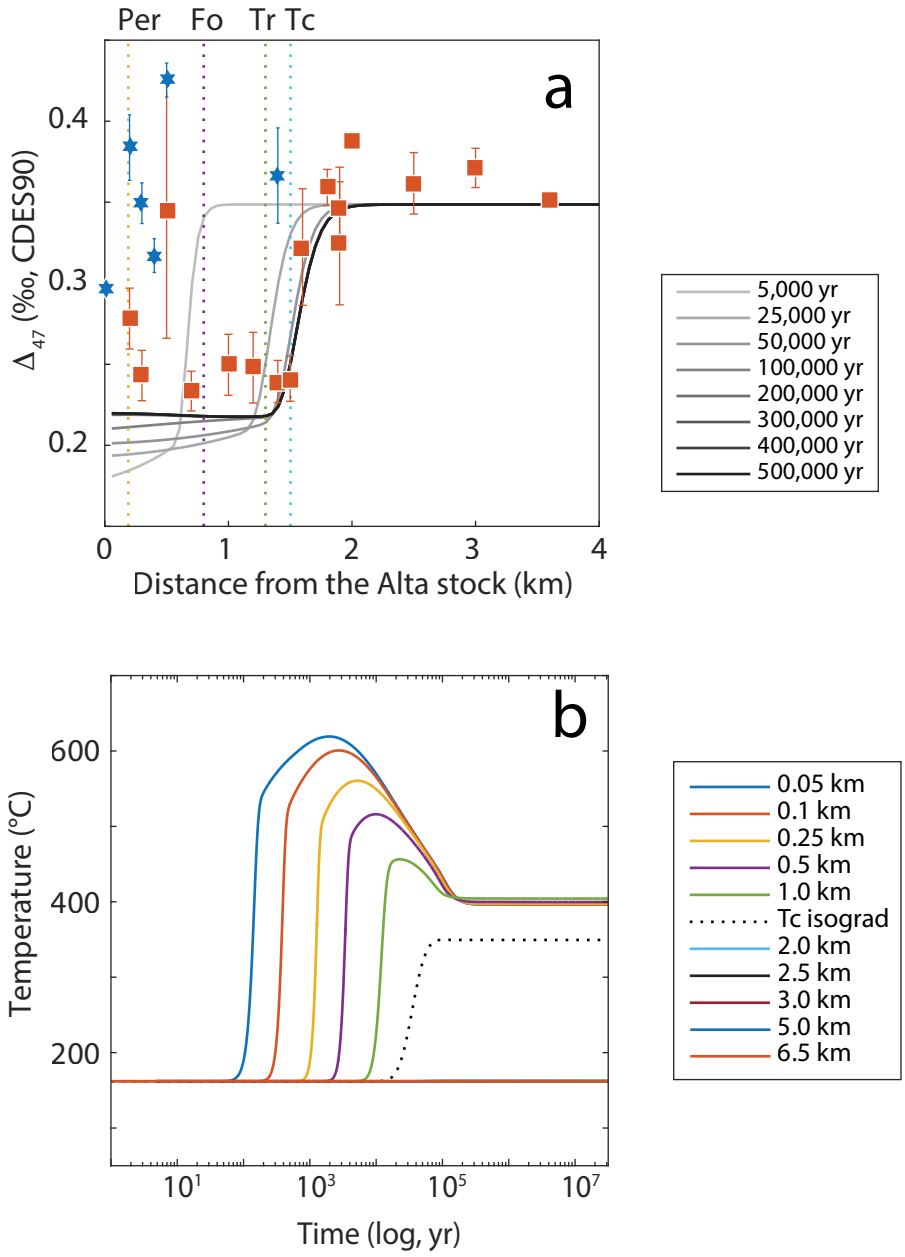

Figure S22. a) Measured dolomite Δ_{47} values, plotted as a function of distance from the Alta stock (symbols), compared to modeled Δ_{47} values (curves) 5,000–500,000 yr after stock emplacement for sampling transect initial temperature (T_i) of 160 °C and Tc isograd maximum temperature (T_{max}) of 400 °C, using the the pseudo-first-order model of Passey and Henkes (2012) and kinetic parameters for dolomite from Monte Carlo simulations of this study. Symbols represent replicate averages. Error bars represent 95% C.I. for replicate analyses or are smaller than symbol size if absent. Vertical dashed lines indicate the approximate location of isograds. b) Modeled $T(\Delta_{47})$ as a function of time (logarithmic scale) after emplacement of the Alta stock using the exhumation history of Armstrong et al. (2003). Curves represent distances from the Alta stock of 0.05–6.5 km. The dashed black curve represents the talc isograd. The grey region represents the $T(\Delta_{47})$ range of the metamorphic aureole.

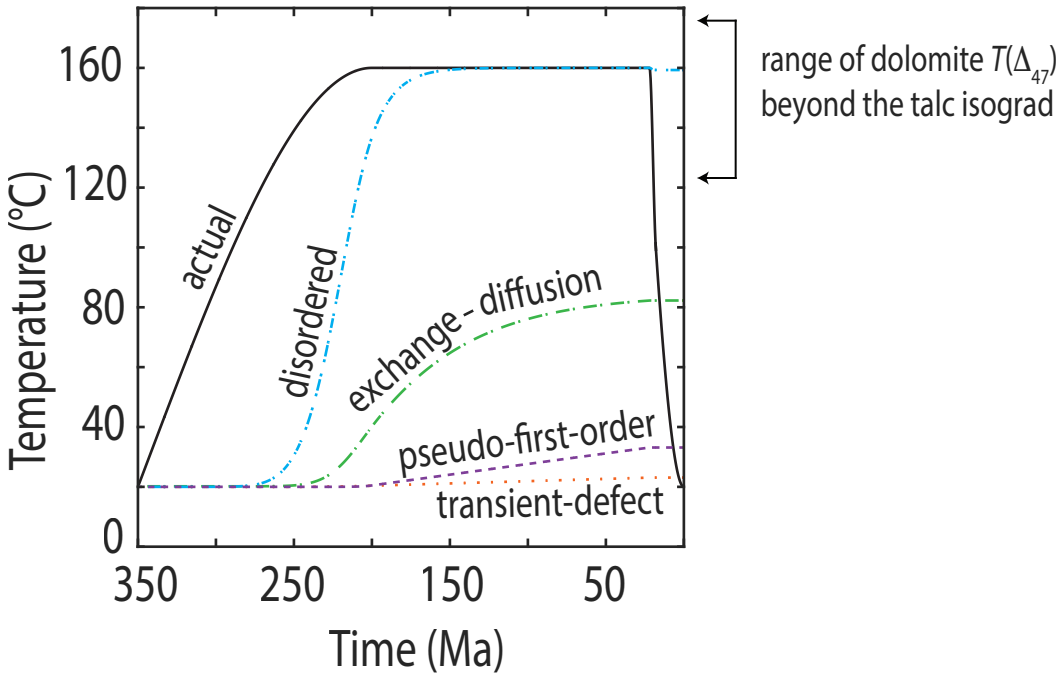

Figure S23. Theoretical simple burial and exhumation history after Armstrong et al. (2003) in the absence of contact metamorphism associated with emplacement of Alta stock. Curves represent actual temperature, solid black curve, and modeled $T(\Delta_{47})$ for a) the pseudo-first-order model of Passey and Henkes (2012), purple dashed curve; b) the transient-defect model of Henkes et al. (2014), orange dotted curve; c) the exchange-diffusion model of Stopler and Eiler (2015), green dotted-dashed curve; and d) the disordered model and kinetic parameters of Hemingway and Henkes (2020), blue dotted-dashed curve. The exchange-diffusion and pseudo-first-order models predict only partial reordering. See supporting information S2 for modeling specifics.

Sample	$\Delta_{48,\ raw}$ *	$\delta^{13}C$ (‰) VPDB	error†	$\delta^{18}O$ (‰) VPDB	error†	Δ_{47}‡ (‰) CDES90	Δ_{47}‡ (‰) CDES25	error†
calcite								
AS17-74	-9.326	-2.70	a	-20.46	b	0.291	0.373	a
	-10.926	-2.75	a	-20.61	b	0.300	0.382	b
	-0.343	-2.43	b	-19.70	b	0.297	0.379	c
AS17-37b	242.681	5.55	a	-9.05	b	0.333	0.415	b
	-0.162	5.80	b	-8.23	b	0.312	0.394	c
	-0.239	5.83	b	-8.27	a	0.312	0.394	c
	-0.227	5.82	b	-8.20	b	0.311	0.394	d
AS17-68w	-4.372	-0.42	a	-11.03	b	0.387	0.469	b
	-3.451	-0.33	a	-11.20	b	0.319	0.401	b
	11.110	-0.36	a	-11.14	b	0.343	0.425	b
	0.000	-0.23	a	-10.80	a	0.392	0.474	d
	-0.180	-0.25	b	-10.82	b	0.392	0.474	d
dolomite								
AS17-39	-1.124	1.06	a	-6.27	b	0.247	0.329	b
	0.965	1.08	a	-6.19	b	0.232	0.314	b
	-0.220	1.18	b	-5.91	a	0.221	0.303	c
	-0.241	1.19	b	-5.81	b	0.249	0.331	c
	-0.160	1.19	c	-5.75	b	0.219	0.301	d
AS17-70	274.124	2.69	a	-2.22	b	0.255	0.337	b
	-0.103	2.73	b	-2.77	b	0.263	0.345	c
	-0.160	2.71	b	-2.81	b	0.231	0.313	c
AS17-44	127.341	5.06	a	-6.45	b	0.234	0.316	b
	-0.222	5.06	a	-6.12	a	0.270	0.352	d
	-0.191	2.36	b	-6.09	b	0.240	0.322	c
AS17-68g	153.334	1.89	a	-3.39	b	0.260	0.342	b
	119.521	2.01	a	-4.15	b	0.241	0.323	b
	-0.236	2.10	b	-3.93	a	0.229	0.311	c
	-0.162	2.10	b	-3.78	b	0.245	0.327	c
AS17-24	18.010	2.73	a	-2.30	b	0.262	0.344	b
	-0.225	2.73	c	-2.15	b	0.238	0.321	c
	-0.179	2.76	b	-2.08	b	0.231	0.313	c
	-0.191	2.76	b	-2.13	b	0.233	0.315	c
AS17-26	6.795	3.08	a	-0.14	b	0.359	0.441	b
	-0.181	3.18	b	0.17	b	0.306	0.388	c
	-0.231	3.18	b	0.26	b	0.302	0.385	c
AS17-28	385.760	2.93	a	-4.35	b	0.355	0.437	b
	36.964	2.48	a	-7.32	b	0.352	0.434	b
	-0.061	2.57	b	-6.93	b	0.370	0.453	c
AS17-57	234.610	3.09	a	-2.68	b	0.344	0.426	b

	-0.239	3.18	b	-2.12	b	0.305	0.388	c
AS17-31b	50.591	1.94	b	-1.19	b	0.359	0.441	b
	-0.194	1.97	b	-0.72	b	0.333	0.415	c
AS17-29	372.610	3.15	a	0.17	b	0.388	0.470	b
	135.612	3.05	b	-0.04	b	0.389	0.471	b
	-0.208	3.13	b	0.42	b	0.385	0.468	c
AS17-60	133.377	1.90	b	-0.57	b	0.352	0.434	b
	-0.157	2.01	b	0.00	b	0.371	0.454	c
AS17-63	42.858	1.83	a	-2.74	b	0.365	0.447	b
	-0.131	1.79	c	-2.84	b	0.377	0.460	c
AS17-65	41.346	2.39	a	-0.65	b	0.353	0.435	b
	-0.227	2.48	b	-0.11	b	0.351	0.367	c
standards[§]								
Carrara	3.173	1.82	0.28	-2.18	0.17	0.366	0.448	0.073
Ooids	10.48	4.71	0.18	0.01	0.40	0.619	0.702	0.022
NBS-19	-0.12	2.00	0.003	-2.06	0.05	0.319	0.401	0.015
102-GC-AZ01	-0.10	0.73	0.06	-14.30	0.08	0.614	0.697	0.009

Note: White background indicates Stable Isotope Laboratory (SIL) and grey background indicates Isotopologue Paleosciences Laboratory (IPL). Data was collected during a single analytical session for each laboratory.

* Raw value indicates averaged value from multiple cycles of sample gas versus reference gas comparisons for a single analysis. See text for details.

† Reported uncertainty is one standard error (± 1 S.E.) of multiple cycles of sample gas versus reference gas comparisons for a single analysis where a is ≤0.001, b is ≤0.005, c is ≤0.010, and d is ≤0.015.

‡ Values are reported in the carbon dioxide equilibrium scale (CDES) after Dennis et al. (2011), using either the 90 °C (CDES90) or 25 °C (CDES25) acid fractionation equivalent value.

§ Reported uncertainty is the 95 percent confidence level (± 95% C.I.) of all replicates (*N*) of a single sample.

Table S1. Values of $\delta^{13}C$, $\delta^{18}O$, Δ_{47}, and Δ_{48} for calcite and dolomite analyzed in both the Stable Isotope Laboratory (SIL) and the Isotopologue Paleosciences Laboratory (IPL).

Sample	SIL only Δ_{47}* (‰) CDES90	*N*	error†	IPL only Δ_{47}* (‰) CDES90	*N*	error†	All Data Δ_{47}* (‰) CDES90	error†
calcite								
AS17-74	0.296	2	0.009	0.297	1	-	0.296	0.005
AS17-37b	0.333	1	-	0.312	3	0.0004	0.317	0.010
AS17-68w	0.350	3	0.039	0.392	2	0.0002	0.366	0.029
dolomite								
AS17-39	0.240	2	0.015	0.229	3	0.019	0.233	0.012
AS17-70	0.255	1	-	0.247	2	0.031	0.250	0.019
AS17-44	0.234	1	-	0.255	2	0.030	0.248	0.022
AS17-68g	0.251	2	0.019	0.237	2	0.013	0.244	0.013
AS17-24	0.262	1	-	0.234	3	0.004	0.241	0.014
AS17-26	0.359	1	-	0.304	2	0.003	0.322	0.036
AS17-28	0.354	2	0.003	0.370	1	-	0.359	0.011
AS17-57	0.344	1	-	0.305	1	-	0.325	0.038
AS17-31b	0.359	1	-	0.333	1	-	0.346	0.026
AS17-29	0.389	2	0.001	0.385	1	-	0.387	0.002
AS17-60	0.352	1	-	0.371	1	-	0.362	0.019
AS17-63	0.365	1	-	0.377	1	-	0.371	0.012
AS17-65	0.353	1	-	0.351	1	-	0.352	0.002

* Values are reported in the carbon dioxide equilibrium scale (CDES) after Dennis et al. (2011), using the 90 °C (CDES90) acid fractionation equivalent value.
† Reported uncertainty is the 95 percent confidence level (± 95% C.I.) of all replicates (*N*) of a single sample.

Table S2. Averaged Δ_{47} values for calcite and dolomite analyzed in both the Stable Isotope Laboratory (SIL) and the Isotopologue Paleosciences Laboratory (IPL). Data within each lab was collected in a single analytical session.

Unit:	1	2	3	4	5	reference(s)
ρ (kg/m^3)	2650	2400	2400	2750	2700	Vilà et al. (2010)
A (W/m^3) × 10^{-6}	0.57	1.16	0.416	0.83	1.82	Vilà et al. (2010), Furlong et al. (1991), Hasterok and Webb (2017)
Cp (coefficients)						Nabelek et al. (2012)
a	1442.6	1916.2	1946.3	1916.2	1916.2	
b	0.0594	-0.0391	-0.0266	-0.0391	-0.0391	
c × 10^{-6}	0	2.197	0	2.197	2.197	
d × 10^{-4}	0	-2.017	-1.847	-2.017	-2.017	
α (coefficients)						Nabelek et al. (2012)
e	0.3	0.534	0.365	0.534	0.534	
f	0	5.017	6.953	5.017	5.017	
g	0	222.1	225.2	222.1	222.1	
depth (km)	5–8	1–1.4	1.4–4.2	4.2–5.5	5.5–8	Cook and Bowman (1994)

Note: Unit number are as follows: 1=volcanics, 2=clastic, 3=carbonate, 4=quartzite, and 5=granodiorite.

Table S3. Thermal properties used in conductive and fluid advective modeling simulations.